

The HERMES Recoil Detector:
Particle Identification and
Determination of Detector Efficiency of
the Scintillating Fiber Tracker

Diplomarbeit
am Institut für Experimentalphysik
der Universität Hamburg

vorgelegt von
Xianguo Lu
aus Shunde, China

Hamburg
September 2009

Gutachter der Diplomarbeit:

Dr. W.-D. Nowak

Prof. Dr. P. Schleper

Abstract

HERMES is a fixed target experiment using the HERA 27.6 GeV polarized electron/positron beams. With the polarized beams and its gas targets, which can be highly polarized, HERMES is dedicated to study the nucleon spin structure. One of its current physics programs is to measure deeply virtual Compton scattering (DVCS). In order to detect the recoiling proton the Recoil Detector was installed in the target region in the winter of 2005, taking data until the HERA-shutdown in the summer of 2007.

The Recoil Detector measured energy loss of the traversing particles with its sub-detectors, including the silicon strip detector and the scintillating fiber tracker. This enables particle identification for protons and pions. In this work a systematic particle identification procedure is developed, whose performance is quantified.

Another aspect of this work is the determination of the detector efficiency of the scintillating fiber tracker.

Kurzfassung

HERMES ist ein Fixed-Target-Experiment zur Untersuchung des Nukleonenspins. Der 27.6 GeV polarisierter Elektron-/Positron-Strahl von HERA wurde auf das hoch polarisierbare Gastarget geleitet. Eines der aktuellen Physikprogramme bei HERMES ist die Messung der tief virtuellen Compton-Streuung (DVCS). Um das rückgestreute Proton nachzuweisen wurde im Winter 2005 der Recoil-Detektor um das Target installiert, der bis zum HERA-Shutdown im Sommer 2007 Daten genommen hat.

Der Recoil-Detektor maß den Energieverlust der durchgehenden Teilchen mittels eines Silizium-Streifen-Detektors und eines Trackers aus szintillierenden Fasern. Er ermöglicht so eine Teilchenidentifizierung für Protonen und Pionen. In dieser Arbeit wurde ein systematisches Teilchenidentifizierungsverfahren entwickelt, dessen Leistung quantitativ beschrieben wird.

Ein anderer Aspekt dieser Arbeit ist die Bestimmung der Detektoreffizienz des Szintillierenden-Fasern-Trackers.

Contents

Contents	i
1 Introduction	1
1.1 Deeply Virtual Compton Scattering — towards the angular momenta of partons in the nucleon	1
1.2 Measurement of DVCS at HERMES	3
2 The HERMES Recoil Detector	6
3 Energy loss of heavy charged particles in the Recoil Detector	10
3.1 The Landau distribution	10
3.2 Extraction of the energy loss distribution from real data	11
3.2.1 Sample selection	11
3.2.2 Incident angle correction	11
3.2.3 Background reduction	13
3.2.4 Fit to the energy loss vs. velocity spectra	14
4 Particle identification with the Recoil Detector	17
4.1 General particle identification formalism	17
4.1.1 Computational techniques	18
4.2 Results	19
4.3 Comparison with conventional procedure	20
4.4 Handling of special cases	24
5 Determination of detector efficiency of the scintillating fiber tracker	27
5.1 Reconstruction of traversing particles	27
5.2 Identification of detected particles	28
5.3 Efficiency calculation	31
5.4 Results	36
6 Summary and conclusion	45
A Energy loss distribution extracted from Monte Carlo data and the corresponding particle identification results	47
B Color plots for efficiency of the scintillating fiber tracker	50

CONTENTS

Bibliography	58
Acknowledgements	60

Chapter 1

Introduction

1.1 Deeply Virtual Compton Scattering — towards the angular momenta of partons in the nucleon

After Rutherford's pioneering experiment, scattering processes have been used to investigate the proton properties and its structure: from elastic scattering of electrons off protons, the electric charge distribution and the magnetic moment of the proton were determined by measuring the electric and magnetic form factors, respectively [Hu65]; from inclusive Deep Inelastic Scattering (DIS) Parton Distribution Functions (PDFs), which can be interpreted as parton densities depending on the longitudinal momentum fraction in the proton, were extracted by determining the structure functions of the proton [Ams08].

These experiments utilized virtual photons as a probe for the proton and its constituents. In constructing the form of the interaction, symmetries like Lorentz covariance are used and the underlying physics associated with the proton is encoded in the electric and magnetic form factors as well as the structure functions. Such formalism is generalized in a larger framework, the Generalized Parton Distributions (GPDs, for review see Refs. [Die03, Goe01]), from which more information about the proton structure like the total angular momenta of partons can be determined.

In elastic scattering, the virtual photon transfers its four-momentum to the proton which therefore transits from the initial state $|P\rangle$ to the final state $|P'\rangle$ with momentum P and P' . The electromagnetic current of the proton j^μ between the two states can be formally written as

$$\langle P'|j^\mu|P\rangle = \bar{u}(P') \left[F_1(\Delta^2)\gamma^\mu + F_2(\Delta^2)\frac{i\sigma^{\mu\nu}\Delta_\nu}{2M} \right] u(P), \quad (1.1)$$

with Dirac spinor u , the gamma matrix γ^μ , and the proton mass M . Here $\sigma^{\mu\nu} = \frac{i}{2}(\gamma^\mu\gamma^\nu - \gamma^\nu\gamma^\mu)$, $\Delta \equiv P' - P$. F_1 and F_2 are called the Dirac and Pauli form factors, respectively. The electric form factor G_E and the magnetic form factor G_M are defined as:

$$G_E(\Delta^2) \equiv F_1(\Delta^2) + \frac{\Delta^2}{4M^2}F_2(\Delta^2), \quad (1.2)$$

$$G_M(\Delta^2) \equiv F_1(\Delta^2) + F_2(\Delta^2). \quad (1.3)$$

In the forward limit where $\Delta^2 \rightarrow 0$, $\langle P'|j^\mu|P\rangle \rightarrow \langle P|j^\mu|P\rangle$, it can be shown that (see e.g. Ref. [Gre03])

$G_E(0) = F_1(0)$ is the proton charge in units of elementary electric charge and
 $G_M(0) = F_1(0) + F_2(0)$ is the magnetic moment of the proton in units of nuclear magneton.

Independent of the scattering process, the formalism described above can be generalized to the quark and gluon parts of the energy-momentum tensors $T_{q,g}^{\mu\nu}$ in Quantum Chromodynamics (QCD). By defining the form factors $A_{q,g}$, $B_{q,g}$ and $C_{q,g}$, which are included in the GPD framework for quarks (q) and gluons (g), in the following way:

$$\langle P'|T_{q,g}^{\mu\nu}|P\rangle = \bar{u}(P') \left[A_{q,g}(\Delta^2) \gamma^{(\mu} \bar{P}^{\nu)} + B_{q,g}(\Delta^2) \bar{P}^{(\mu} i\sigma^{\nu)\alpha} \Delta_\alpha / 2M + C_{q,g}(\Delta^2) \Delta^{(\mu} \Delta^{\nu)} / M \right] u(P), \quad (1.4)$$

where $\bar{P}^\mu = (P^\mu + P'^\mu)/2$ and $(\mu\nu)$ denotes symmetrization with respect to μ, ν indices (i.e. $a^{(\mu}b^{\nu)} = a^\mu b^\nu + a^\nu b^\mu$), Ji showed that [Ji97, Ji98]

$A_{q,g}(0)$ give the charges of the energy-momentum currents — the energy-momentum fractions carried by quarks and gluons¹, and
 $A_{q,g}(0) + B_{q,g}(0)$ give the fractions of the total angular momenta:

$$J_{q,g} = \frac{1}{2} \left[A_{q,g}(0) + B_{q,g}(0) \right]. \quad (1.5)$$

One could expect to be able to extract $J_{q,g}$ if there were a practical experimental probe coupling to the quark and gluon energy-momentum tensors like a virtual photon coupling to the proton electromagnetic current. Nevertheless, the energy-momentum tensors do appear in the operator product expansion (OPE) in calculating the amplitude for hard Compton scattering off the proton

$$\gamma(q)p(P) \rightarrow \gamma(q')p(P') \quad (1.6)$$

with q (q') being the momenta of the incoming (outgoing) photons and $|q^2| \gg 1$ (GeV/c)² (see e.g. Ref. [Pes95]). Figure 1.1 shows the corresponding Feynman diagram and its leading order contribution. However in inclusive DIS ($\gamma p \rightarrow f$ with any final state f), whose cross section via the optical theorem is related to the amplitude of Eq. 1.6 with $q = q'$ and $P = P'$, $B_{q,g}$ cannot be extracted because its contribution is eliminated at zero momentum transfer to the proton ($\Delta = P' - P = 0$ in Eq. (1.4)).

¹Consider PDFs $f_q(x)$ ($-1 < x < 1$) which give the quark and antiquark densities in the longitudinal momentum fraction $|x|$ as $f_q(x)$ ($0 < x < 1$) and $-f_q(x)$ ($-1 < x < 0$), respectively. It is interesting to note that,

$$\int_{-1}^1 dx f_q(x) = N_q, \quad \int_{-1}^1 dx x f_q(x) = A_q(0).$$

Here, as the partonic version of $F_1(0)$, N_q is the net number of quarks of flavor q . On the other hand, in the language of operator product expansion (OPE), the current and the energy-momentum tensor corresponding to N_q and A_q are twist-2 (i.e. leading contribution in the expansion of an operator product) spin-1 and twist-2 spin-2 operators, respectively. Roughly speaking, GPDs generalize PDFs in the sense that they depend on two more variables which account for their off-forward nature (non-zero Δ). With zero Δ , they reduce to PDFs. GPDs are related to form factors of twist-2 spin- n operators in a similar fashion as above through their n th Mellin moments in x .

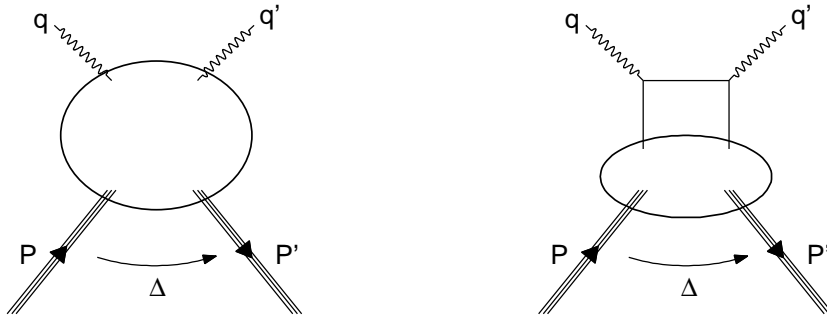


Figure 1.1: *Left*: hard Compton scattering. *Right*: its leading order diagram.

One of the solutions is to measure the Deeply Virtual Compton Scattering (DVCS) (Eq. 1.6) with a virtual incoming photon and a real outgoing one. Because in this process $P \neq P'$, results need to be extrapolated to the forward limit [Ji97, Ji98]. In recent years, many experimental attempts have focused on this [Sau99, Air01, Ste01, Air08].

1.2 Measurement of DVCS at HERMES

HERMES is a fixed target experiment studying the nucleon spin structure [Ack98, Air05, Air07]. It was located in the east hall of the HERA 27.6 GeV electron/positron storage ring in Hamburg, Germany. It used polarized electron/positron beams to scatter off polarized or unpolarized hydrogen, deuterium, and helium-3 targets, as well as some other unpolarized nuclear gas targets. It consisted of a forward spectrometer and after the year of 2005 a Recoil Detector enclosing the target cell. Figure 1.2 shows a side view of the detectors. The spectrometer was symmetric in its upper and bottom halves. It consisted of a dipole magnet, tracking chambers, a Ring Imaging CHerenkov (RICH) detector, a Transition Radiation Detector (TRD) and an electromagnetic calorimeter with a preshower detector in front.

In the measurement of DVCS, HERMES detected the scattered beam lepton by the tracking system together with TRD, the preshower detector and the calorimeter, and also detected the real photon by the calorimeter. The kinematics of the recoiling target proton is constrained by that of the scattered lepton and the real photon. It has a momentum up to 1.5 GeV/c with a scattering angle between 0.1 – 1.35 rad [Kai02]. With the front spectrometer alone, HERMES could not detect the recoiling protons. Analyses based on such data were performed by requiring the missing mass (invariant mass of the undetected final state) close to the proton mass [Air08]. As can be seen in Fig. 1.3, a cut on the missing mass removes most of the semi-inclusive background ($ep \rightarrow e\gamma X$). However, the residual semi-inclusive background and the background from nucleon resonance ($ep \rightarrow e\gamma\Delta^+$) still contributes significantly.

At the end of 2005, the Recoil Detector was installed to detect directly the recoiling proton and to reject the resonance state by their decay products [Kai02]. With the measured momenta of the particles in the Recoil Detector acceptance, recoiling protons can be selected by kinematic constraints. Real data analysis using conventional particle identification (PID) with the Recoil Detector [Lu08] (see Section 4.3) shows that additional information from PID improves the selection of recoiling protons [Yu09]. In Fig. 1.4 the missing mass spectra are

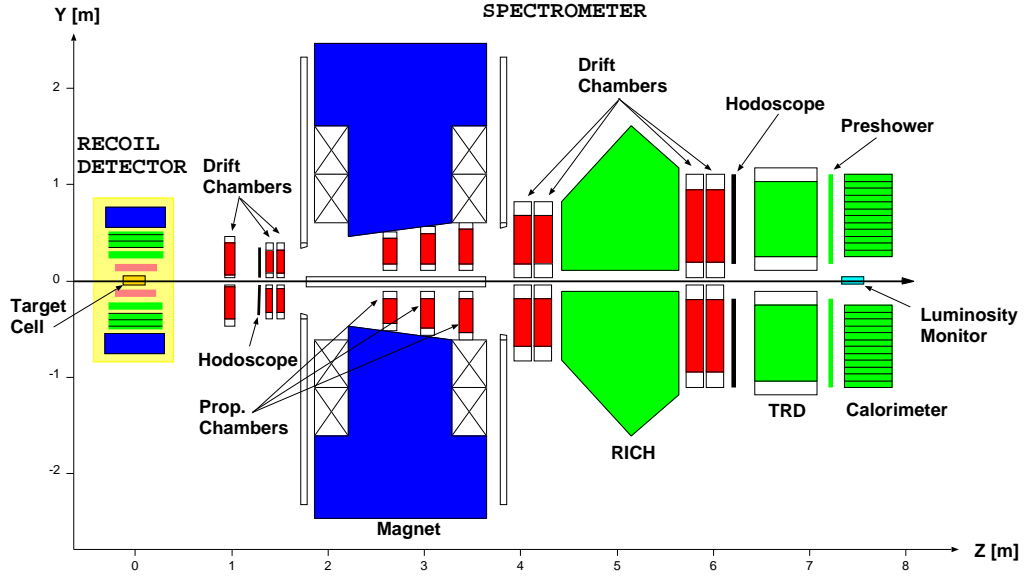


Figure 1.2: A side view of the HERMES spectrometer and the Recoil Detector (configuration for 2006 and 2007). The experiment's (right handed) Cartesian coordinate system has its z -axis along the beam axis and the y -axis pointing upwards. The corresponding spherical coordinates (r, θ, ϕ) are defined in the usual way, i.e. via the following transformation: $x = r \sin \theta \cos \phi$, $y = r \sin \theta \sin \phi$, $z = r \cos \theta$.

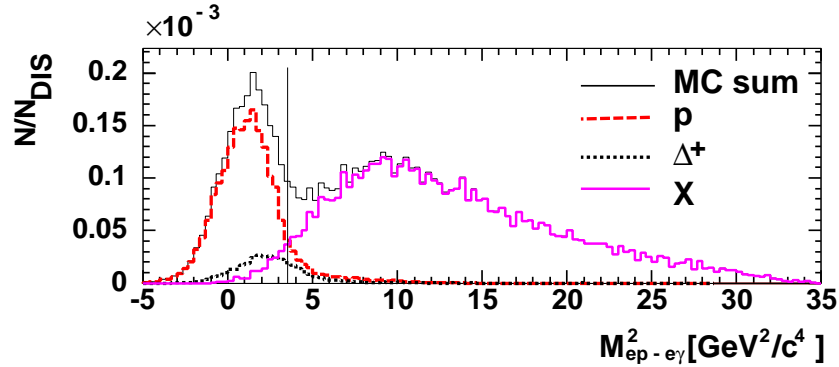


Figure 1.3: Monte Carlo simulations of the missing mass spectra in the front spectrometer acceptance. The dashed red curve corresponds to a missing proton. The dotted black curve corresponds to a missing Δ^+ . All other undetected final states (semi-inclusive background) contribute to the solid magenta curve. The vertical line indicates a cut on the missing mass [E1105].

shown for real data samples selected with different requirements in the Recoil Detector. The proton (solid line) is selected as a positively charged particle which is identified as a proton satisfying certain kinematics constraints. If a positively charged particle is identified as a pion, π^+ is selected (circle points; because of baryon number conservation, some undetected particle X must accompany). The π^+ sample has two contributions, one from Δ^+ decaying to π^+n (branching ratio 33%), the other from the semi-inclusive background which is charge-

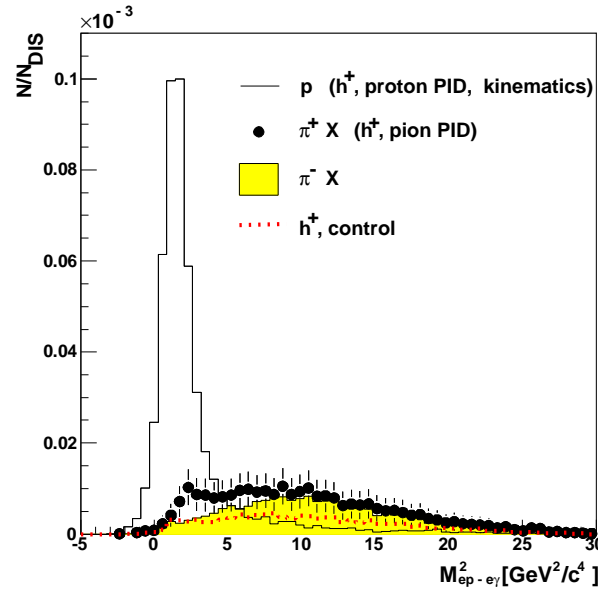


Figure 1.4: Missing mass spectra in the front spectrometer acceptance for data samples selected with different requirements in the Recoil Detector [Yu09].

symmetric and can be estimated by selecting π^- (shaded yellow region; in the Recoil Detector negatively charged particles detected are mostly pions, see Section 3.2.3). The difference between the $\pi^+ X$ and $\pi^- X$ samples comes from the $\Delta^+ \rightarrow \pi^+ n$ decay. For comparison, a control sample of positively charged particles, which are identified neither as protons nor as pions, is also shown, where no peak is seen as expected.

Techniques used in the conventional PID with the Recoil Detector prohibit a quantitative estimation for the PID performance. In this work new techniques for a systematic PID procedure are developed, which allow the identification efficiency and contamination to be quantified.

In this thesis, the PID procedure described is based on the energy loss measured by the Recoil Detector. After a basic introduction to the Recoil Detector in Chapter 2, the extraction of the energy loss is described in Chapter 3. The formalism and technical details of the PID procedure are then described in Chapter 4.

Another aspect of this work is to determine the detector efficiency of one of the sub-detectors of the Recoil Detector — the scintillating fiber tracker. This is presented in Chapter 5.

Chapter 2

The HERMES Recoil Detector

The Recoil Detector installed in the target region in front of the spectrometer consists of three sub-detectors — the silicon strip detector, the scintillating fiber (SciFi) tracker and the photon detector — inside a 1 Tesla superconducting solenoid (Fig. 2.1). In order to detect protons with very low momenta, the innermost tracking component — the silicon detector — was placed inside the beam vacuum, directly surrounding the target cell. Protons with momenta down to 125 MeV/c can be detected. The Recoil Detector has an acceptance in θ between 0.3 – 2.5 rad. Because of the passive holding structure of the silicon detector, 25% of the 2π acceptance in azimuthal angle ϕ is inaccessible [Kai02, Mus08]. Figure 2.2 shows a cross sectional view of the detector. It can be seen that the detector is symmetric under $\pi/2$ -rotations, and the four quadrants (Q1–4) can be considered as four individual detection systems.

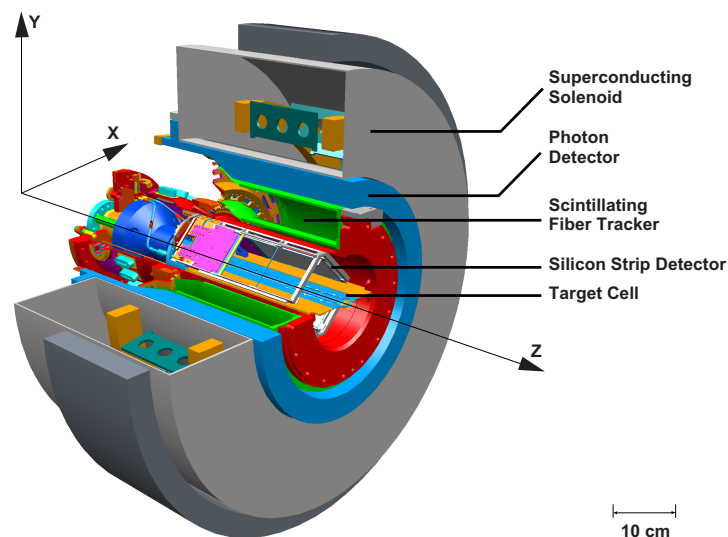


Figure 2.1: A CAD model of the Recoil Detector.

The silicon detector [Pic08] consists of 16 double-sided sensors mounted on 8 modules which are arranged in 2 layers (ISSD, OSSD). Being $300\ \mu\text{m}$ thick, each sensor has an active area of $9.9\ \text{cm} \times 9.9\ \text{cm}$ and a pitch of $758.2\ \mu\text{m}$. Figure 2.3 shows a sketch of the two sides of one module. The strips on the p-side (n-side) are oriented parallel (perpendicular) to the beam axis. Each strip is connected via the Kapton flex-foils to two HELIX input channels, to

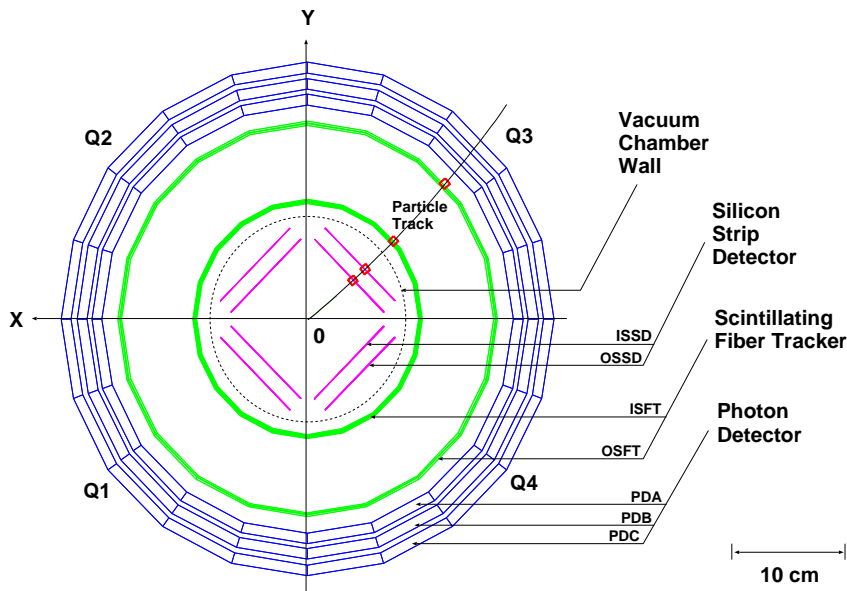


Figure 2.2: A cross sectional view of the Recoil Detector. A particle track with its space points (red squares) is shown.

which the signal is divided with a ratio of 1 : 5 into a low gain (LG) component and a high gain (HG) component. This split up allows to read out signals with a large dynamic range. From the fired strips on both sides of the sensor, space points can be determined. Two space points can be measured for a track traversing the silicon detector.

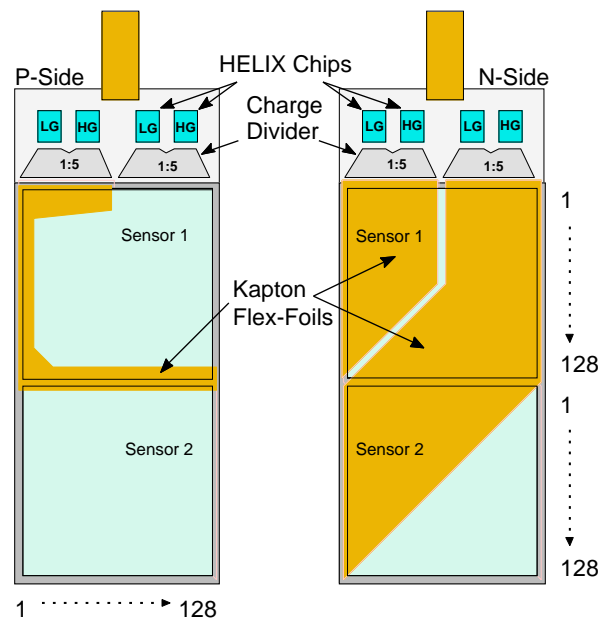


Figure 2.3: A sketch of the two sides of one silicon detector module on which two double-sided sensors are mounted. Signal are routed via Kapton flex-foils to the HELIX readout chips. A charge divider network is integrated with the HELIX chips to increase the dynamic range. The dotted arrows show the numbering of the strips.

The SciFi tracker [Hoe06] consists of four layers of 1 mm diameter scintillating fibers arranged parallel (SFIP, SFOP) or with a stereo angle of 10° (SFIS, SFOS) to the z -axis (Fig. 2.4 *left*). The four layers, which are grouped into two barrels (ISFT, OSFT), are each made up of two sub-layers as shown in the right panel of Fig. 2.4. Traversing particles deposit energy in the fibers producing scintillation light that is transported by light guides and subsequently converted to electronic signals by photomultiplier tubes (PMTs). Individual readout channels are equipped for the ISFT sub-layers SF11-4 as well as for SFOP and SFOS. In total two space points can be formed for a traversing track, each in one barrel, by combining signals from the parallel and stereo layers.

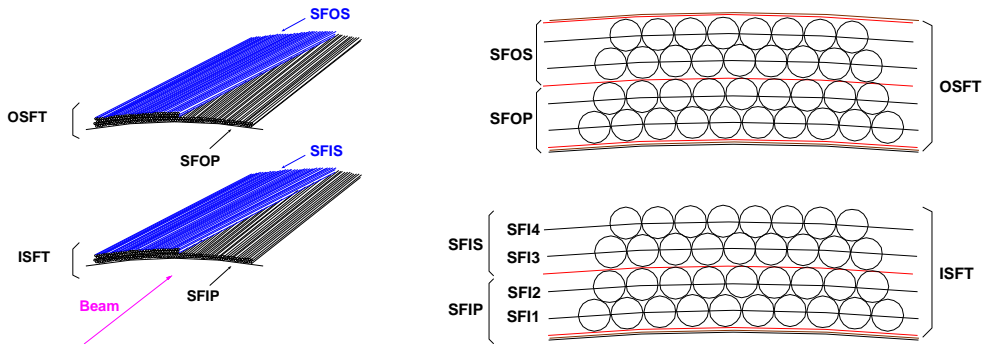


Figure 2.4: Layer configuration of the SciFi tracker.

The photon detector [Van07] is a sampling calorimeter consisting of 3 tungsten/scintillator layers (PDA-C). It is designed to detect the photons from the decay of the Δ^+ -resonance ($\Delta^+ \rightarrow p\pi^0 \rightarrow p\gamma\gamma$) which can not be ruled out by the silicon detector and the SciFi tracker.

From the N ($2 \leq N \leq 4$) space points measured by the silicon detector and the SciFi tracker, particle tracks, correspondingly called NSP tracks, are reconstructed assuming that the particles originate from the beam. The particle momentum is determined according to the bending in the magnetic field. Further information about multiple scattering and energy loss can be used by imposing different particle hypotheses, of which the proton hypothesis and the pion hypothesis are commonly used. With both hypotheses, correlation between deflection in different layers due to multiple scattering is taken into account. Because the energy loss by slow protons has a strong velocity dependence, track fitting with a proton hypothesis also takes the energy deposit in the silicon detector into account, which improves the momentum determination for true protons but not for true pions. In this work, tracks reconstructed with pion hypothesis are used. The momentum resolution for protons (Fig. 2.5) is about 15%, and is worse in the low momentum region. The momentum resolution for pions is about 10% in the momentum range of 0.2 – 1 GeV/c [Yas09].

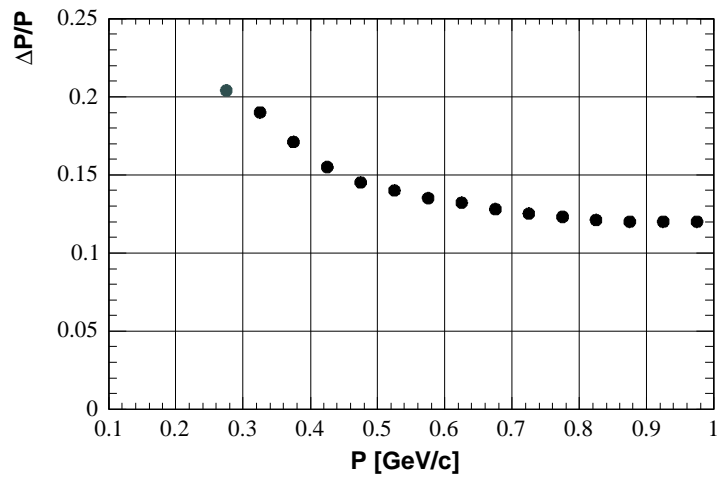


Figure 2.5: Relative momentum uncertainty $\Delta P/P$ of reconstructed proton tracks, as obtained from Monte Carlo simulations [Yas09].

Chapter 3

Energy loss of heavy charged particles in the Recoil Detector

Energy loss in the Recoil Detector is essential for particle identification, as well as for detector efficiency. This chapter is dedicated to the extraction of the energy loss distribution from real data.

3.1 The Landau distribution

Heavy charged particles, like protons or charged pions, lose energy in matter mainly through electromagnetic interaction with atoms. Because of its stochastic nature, the energy loss Δ follows an intrinsic distribution function $F_I(\Delta)$ that depends on the interaction cross section.

For a heavy charged particle of velocity β (in unit of the speed of light) perpendicularly traversing a thin absorber, Landau gave the following equation (for review see Refs. [Fan63, Bic88, Ams08]) for the energy loss distribution¹:

$$F_I(\Delta; \Delta_p, \xi) = \frac{1}{\xi} \frac{1}{2\pi i} \int_{-i\infty}^{+i\infty} e^{u\lambda + u \ln u} du. \quad (3.1)$$

It is parameterized by the Landau parameter ξ and the most probable value² Δ_p through the Landau energy loss variable λ :

$$\xi = \frac{K}{2} \left\langle \frac{Z}{A} \right\rangle \frac{x}{\beta^2}, \quad (3.2)$$

$$\lambda(\Delta) = \frac{\Delta - \Delta_p}{\xi}. \quad (3.3)$$

Here $K = 4\pi N_A r_e^2 m_e c^2$ with Avogadro's number N_A , the classical electron radius r_e and the electron rest energy $m_e c^2$; Z , A and x are atomic number, atomic mass and thickness (in unit of [Density×Length]) of the absorber, respectively; Δ_p is given by

$$\Delta_p = \xi \left[\ln \frac{2m_e c^2 \beta^2 \gamma^2}{I} + \ln \frac{\xi}{I} + j - \beta^2 - \delta(\beta\gamma) \right], \quad (3.4)$$

¹ F_I can be rewritten in the real form $F_I = \frac{1}{\xi} \frac{1}{\pi} \int_0^\infty e^{-u\lambda - u \ln u} \sin \pi u du$.

² F_I peaks at $\lambda = -0.22278$.

where I is the mean excitation energy, $j = 0.200$ [Bic88] and δ is the density correction [Bic88] which can be neglected in the non-relativistic region. Expanding Δ_p to $O(\beta^4)$ gives:

$$\frac{\Delta_p}{\frac{K}{2} \left\langle \frac{Z}{A} \right\rangle x} = \frac{\ln \frac{K \left\langle \frac{Z}{A} \right\rangle x m_e c^2}{I^2} + j}{\beta^2} + \frac{\beta^2}{2} + O(\beta^4). \quad (3.5)$$

The $1/\beta^2$ dependence arises from the Rutherford cross section.

In practice, modifications are needed. For non-perpendicular traversing, x should be replaced by the path length, which depends on the incident angle. The angular dependence of the energy loss thereby introduced can be eliminated by an incident angle correction (see Section 3.2.2). Further, the measured energy loss generally contains a noise³ ϵ that can be modeled as following a Gaussian distribution with zero mean and a width of σ , $G(\epsilon; 0, \sigma) = (\sqrt{2\pi}\sigma)^{-1} \exp(-\epsilon^2/2\sigma^2)$. The distribution function F of the measured energy loss $\Delta + \epsilon$ is the convolution of F_I and G :

$$F(\Delta + \epsilon) = \int_{-\infty}^{+\infty} F_I(\Delta + \tau; \Delta_p, \xi) G(\epsilon - \tau; 0, \sigma) d\tau. \quad (3.6)$$

In order to simplify notations, from here on, Δ refers to the measured energy loss.

3.2 Extraction of the energy loss distribution from real data

For illustration purpose, all plots shown in this section are only based on quadrant 3 (Q3) tracks, which is from now on chosen to represent the typical results of the analysis.

3.2.1 Sample selection

In this work, energy loss distributions in the Recoil Detector layers are extracted from real data. The following requirements are placed in order to reduce the ghost track contamination:

- only 4SP tracks (see Chapter 2) are selected;
- exactly one track is reconstructed per event.

3.2.2 Incident angle correction

When a particle traverses a detection layer, its path length L varies with different incident angles, which makes the energy loss also dependent on the track parameters θ and ϕ (in the experiment's spherical coordinate system, see Fig. 1.2) as well as on the track radius (in meters) $R = P_T/0.3 = P \sin \theta/0.3$ with momentum P and its transverse component P_T in GeV/c. In particular, L factorizes as $L = x/w(\theta, \alpha) = x/(\sin \theta \cos \alpha)$, where x is the thickness and α is the projection of the incident angle onto the transverse plane to the z -axis. Because Δ_p and ξ scale as $L(a + b \ln L)$ and L respectively with L -independent quantities a and b , the

³This is to be understood as the overall effect of electronic noise, cluster-finding, noise cut, imperfect pedestal subtraction, *etc.*

CHAPTER 3. ENERGY LOSS OF HEAVY CHARGED PARTICLES IN THE RECOIL DETECTOR

angular dependence can be approximately removed by normalizing the energy loss to zero incident angle: $\Delta \rightarrow \Delta \cdot w$.

Compared to R , the layer radius r is a small quantity. To the next to leading order of r/R , $\cos \alpha$ reads⁴:

$$\cos \alpha = \cos \left(\arcsin \frac{r}{2R} \right) \quad (3.7)$$

$$= 1 - \frac{1}{8} \left(\frac{r}{R} \right)^2 + O \left[\left(\frac{r}{R} \right)^4 \right], \text{ for SciFi,} \quad (3.8)$$

$$\cos \alpha = \cos \left[\arcsin \left(\sin \phi' - \frac{r}{R} \right) \right] \quad (3.9)$$

$$= \cos \phi' + \frac{r}{R} \tan \phi' + O \left[\left(\frac{r}{R} \right)^2 \right], \text{ for silicon,} \quad (3.10)$$

where $\phi' = \text{mod}(\phi, \pi/2) - \pi/4$ and R is multiplied by -1 for negatively charged particles. The geometry is shown in Fig. 3.1.

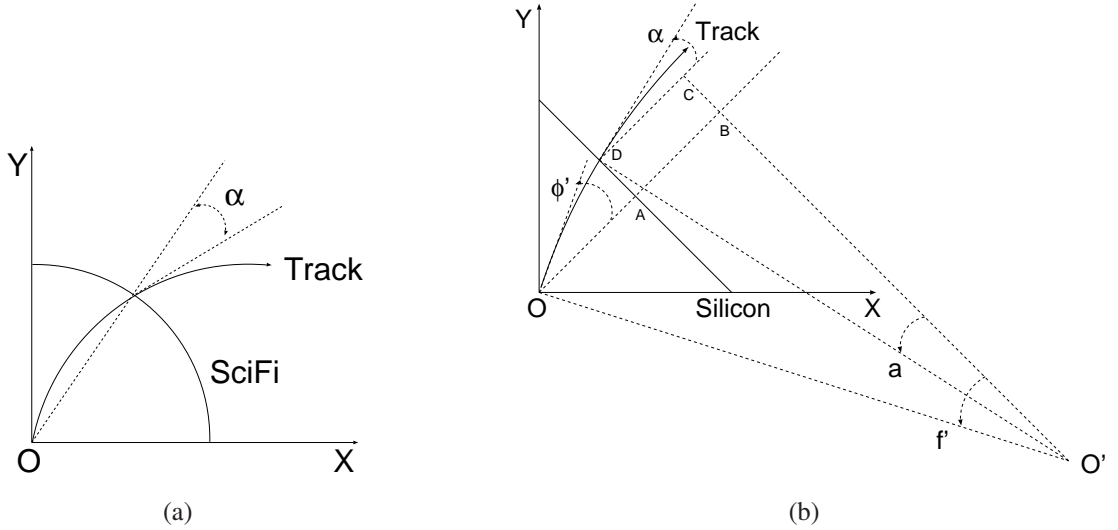


Figure 3.1: View of a track, which traverses the SciFi (a) and silicon (b) layer, along the z -axis. Geometrical relation in (b): $OO' = R$, $R \sin \phi' = OB$, $R \sin \alpha = CD = AB$, $OB - AB = OA = r$.

Figure 3.2 shows the effects of scaling the energy loss only by $\sin \theta$. To this extent, the P_T -dependence is already eliminated. However, as can be seen in Fig. 3.3 left panel, the ϕ' -dependence still exists for the silicon detector. After being scaled additionally by $\cos \phi'$, this ϕ' -dependence is eliminated (Fig. 3.3 right). It can thus be concluded that within the uncertainty of the energy loss measurement (of the order of 20%, see Section 3.2.4), it is sufficient to use $\cos \alpha$ calculated at leading order, i.e. $\cos \alpha = 1$ for the SciFi detector and $\cos \alpha = \cos \phi'$ for the silicon detector.

⁴An offset of the beam in the x - y plane is not considered, i.e. particle tracks are assumed to originate from the z -axis.

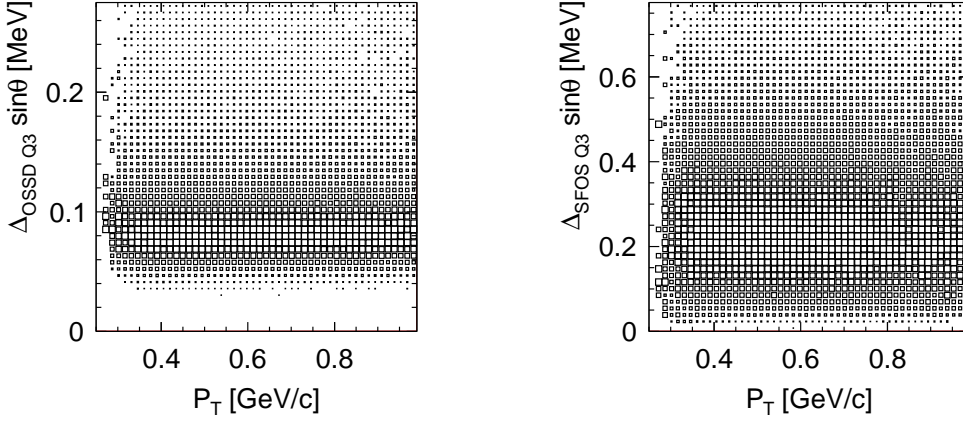


Figure 3.2: Energy loss scaled by $\sin\theta$, in (*left*) OSSD Q3 and (*right*) SFOS Q3 as a function of P_T . Minimum ionizing negative pions ($|P| > 0.6$ GeV/c) are used. It can be seen that the P_T -dependence is eliminated.

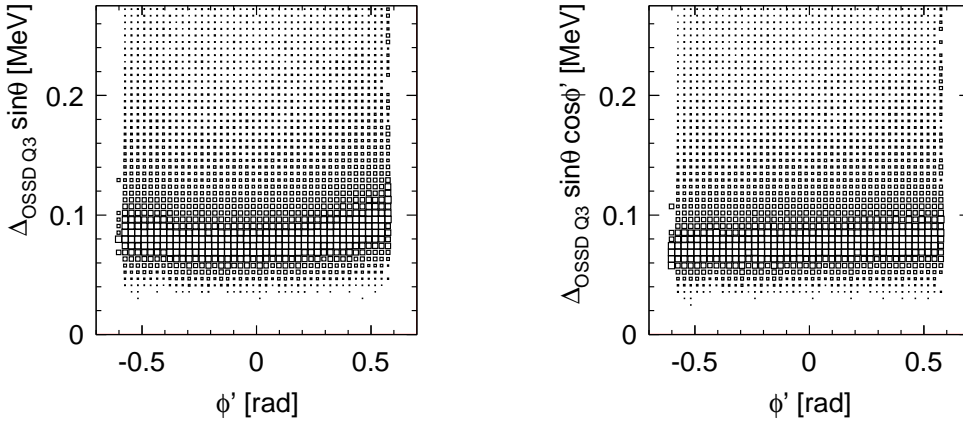


Figure 3.3: Normalized energy loss in OSSD Q3 as a function of ϕ' . The ϕ' -dependence can still be seen if the energy loss is scaled only by $\sin\theta$ (*left*). By an additional scaling factor $\cos\phi'$, the ϕ' -dependence is eliminated (*right*), given the 20% uncertainty of the energy loss measurement (see Section 3.2.4).

3.2.3 Background reduction

In the Recoil Detector acceptance, the major particle types detected are protons and charged pions (Fig. 3.4). By assigning the proton mass to positively charged particles and the pion mass to negatively charged ones, the true Δ vs. β distribution is formed with a background contribution from positive pions due to an incorrect mass assignment. The background can be reduced by rejecting particles with energy loss beyond $\Delta_{p-2\sigma}^{+6\sigma}$ in other layers of the detector. This exploits the fact that energy loss distributions in different layers are uncorrelated. Here Δ_p is the most probable value of the true Δ vs. β distribution and σ is the Gaussian width estimated as 20% Δ_p (Fig. 3.5).

In this $\log_{10}\beta\gamma$ basis, low momentum negative pions overlap with protons. They should be discarded because of their bad momentum resolution. In this work, the following momentum

requirements are applied:

- $|P| > 0.2$ GeV/c for negatively charged particles;
- $|P| < 1.28$ GeV/c for positively charged particles to avoid an overlap with negatively charged ones in the $\log_{10}\beta\gamma$ basis.

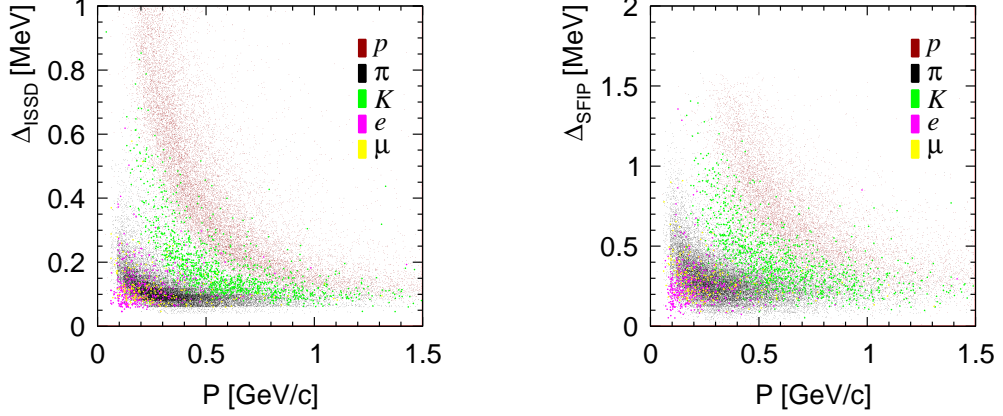


Figure 3.4: Measured energy loss in ISSD (*left*) and SFIP (*right*) against the reconstructed particle momentum, as obtained from Monte Carlo simulations (see Appendix A). Statistics from protons and pions is dominant. (The plot content may only be identified with a color display.)

3.2.4 Fit to the energy loss vs. velocity spectra

The energy loss distribution function $F(\Delta; \beta)$ (Eq. (3.6)) is extracted by least-square fits in $\log_{10}\beta\gamma$ -bins. Examples are shown in Fig. 3.6.

The parameters Δ_p , ξ and σ are further parameterized as functions of β :

$$\Delta_p(\beta; a_{-1}^{\Delta_p}, a_0^{\Delta_p}, a_1^{\Delta_p}) = a_{-1}^{\Delta_p} \cdot \frac{1}{\beta^2} + a_0^{\Delta_p} + a_1^{\Delta_p} \cdot \beta^2, \quad (3.11)$$

$$\xi(\beta; a_{-1}^{\xi}, a_0^{\xi}) = a_{-1}^{\xi} \cdot \frac{1}{\beta^2} + a_0^{\xi}, \quad (3.12)$$

$$\sigma(\beta; a_{-1}^{\sigma}, a_0^{\sigma}, a_1^{\sigma}) = a_{-1}^{\sigma} \cdot \frac{1}{\beta^2} + a_0^{\sigma} + a_1^{\sigma} \cdot \beta^2. \quad (3.13)$$

In practice, the measured energy loss as a sum of all sub-level signals may have systematic deviations from the general theoretical description (Eqs. (3.2) and (3.4)). The parametrization is chosen to retain the basic ingredients like the $1/\beta^2$ terms in Δ_p and ξ , as well as to provide a sufficient number of degrees of freedom to describe the data points (Fig. 3.7). As can be seen from the results, $\sigma \approx 20\% \Delta_p$, which indicates a 20% uncertainty of the energy loss measurement. Consequently, the energy loss distribution $F(\Delta; \beta)$ is fully described by a set of parameters:

$$F(\Delta; \beta) = F(\Delta; \beta; a_{-1}^{\Delta_p}, a_0^{\Delta_p}, a_1^{\Delta_p}, a_{-1}^{\xi}, a_0^{\xi}, a_{-1}^{\sigma}, a_0^{\sigma}, a_1^{\sigma}). \quad (3.14)$$

3.2. EXTRACTION OF THE ENERGY LOSS DISTRIBUTION FROM REAL DATA

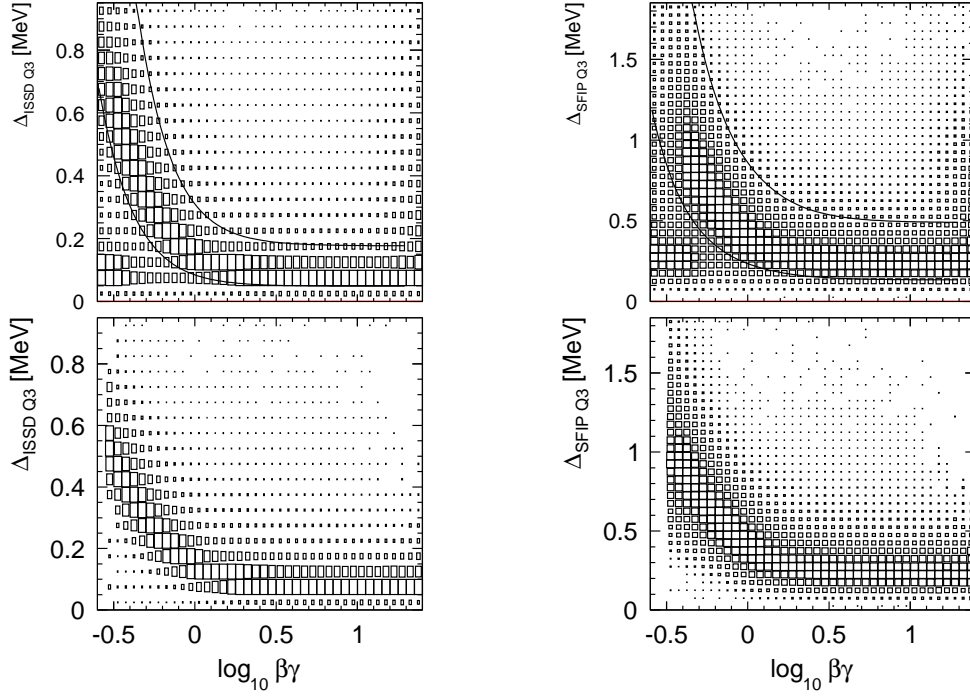


Figure 3.5: *Upper:* The β -dependence of the energy loss in ISSD Q3 (*left*) and SFIP Q3 (*right*). The $\Delta_{p-2\sigma}^{+6\sigma}$ regions are enclosed between the solid lines. Each profile in $\log_{10} \beta\gamma$ is normalized to unity at the maximum. *Lower:* Energy loss distributions in ISSD Q3 (*left*) and SFIP Q3 (*right*) after background reduction.

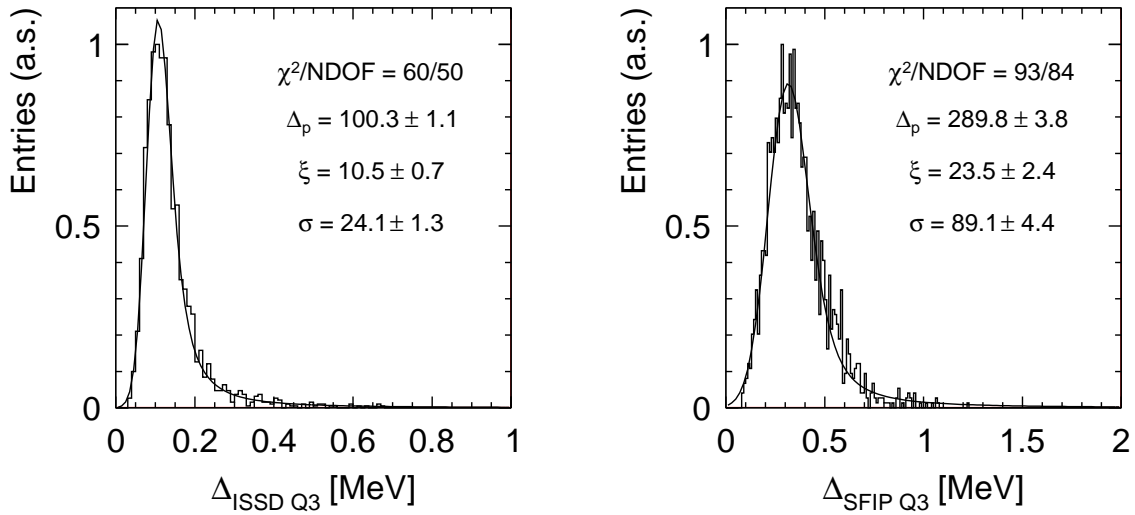


Figure 3.6: Fits to the energy loss distributions in the $\log_{10} \beta\gamma$ -bin 0.17 – 0.18. Entries are in arbitrary scale (*a.s.*). Fitting parameters shown are in keV.

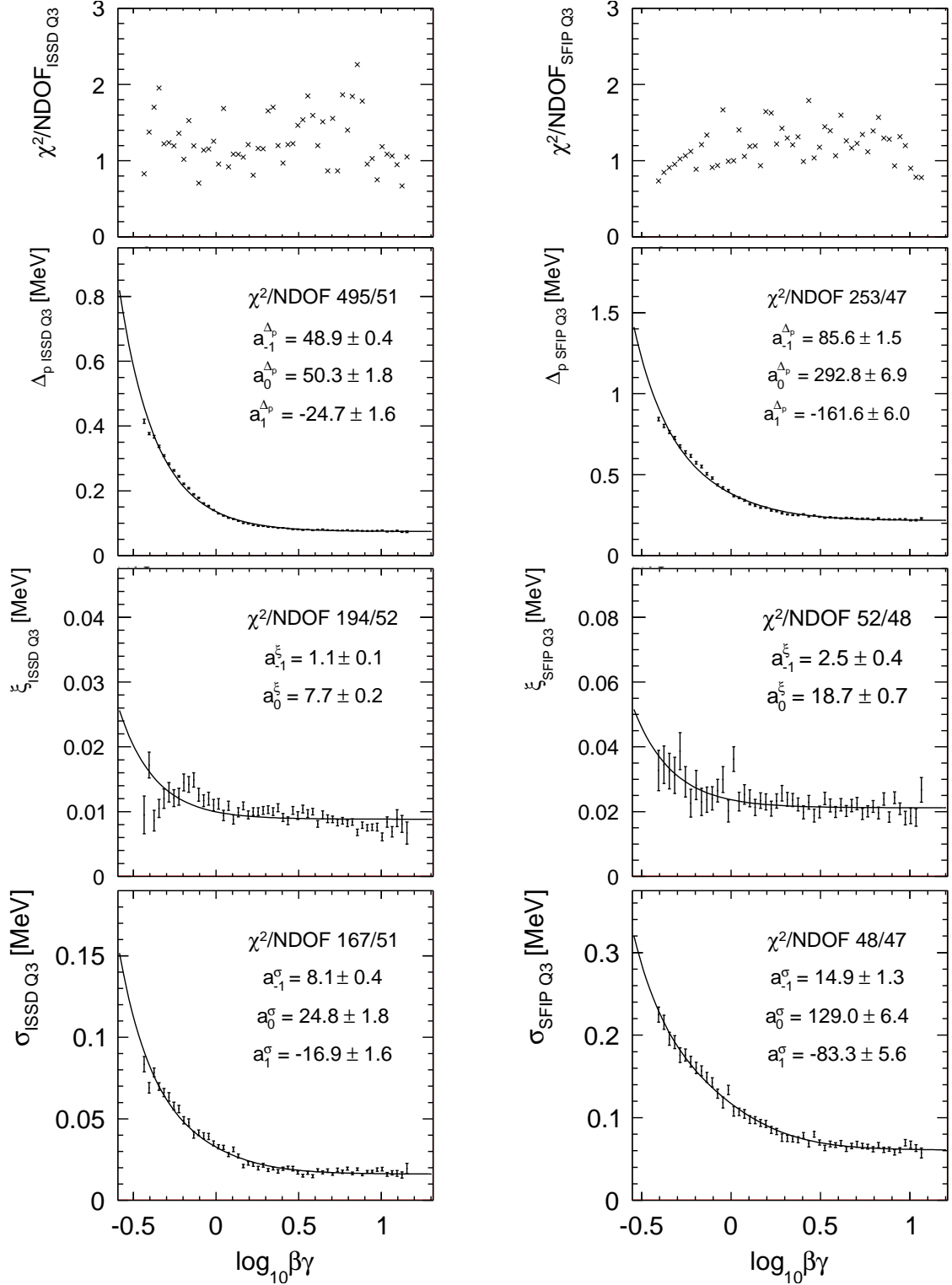


Figure 3.7: *Uppermost:* the quality of fit (measured by χ^2/NDOF) in $\log_{10} \beta\gamma$ -bins. *Lower:* extracted Δ_p , ξ , σ , and the corresponding fits to them. Fitting parameters shown are in keV. The large χ^2/NDOF of the fit to Δ_p indicates that the parameterization in Eq. (3.11) is not perfect given the high statistical accuracy of the extracted data points, whereas the deviation of the fitting curve from the data points is small.

Chapter 4

Particle identification with the Recoil Detector

After the determination of the energy loss distribution function $F(\Delta; \beta)$ (see Chapter 3), a systematic particle identification procedure is described in this chapter. In the Recoil Detector analysis, only protons and charged pions are considered due to their predominant statistics. Particle identification with the Recoil Detector is to identify these two types of particles using energy loss measured by the six layers of the silicon strip detector and the scintillating fiber tracker (ISSD, OSSD, SFIP, SFIS, SFOP, SFOS) separately for each quadrant (Q1–4).

4.1 General particle identification formalism

For a particle traversing several layers of material, the energy loss Δ_L in each layer can be combined after a probabilistic transformation (the subscript L denotes the layer-dependence):

$$\Delta_L \rightarrow \text{PID}_L(\Delta_L; P) \equiv \log_{10} \frac{F_L(\Delta_L; \beta\gamma = \frac{P}{m_p})}{F_L(\Delta_L; \beta\gamma = \frac{P}{m_\pi})}, \quad (4.1)$$

$$\text{PID}(\vec{\Delta}; P) \equiv \sum_L \text{PID}_L(\Delta_L; P), \quad (4.2)$$

where P is the particle momentum, m_p (m_π) is the proton (pion) mass and $\vec{\Delta}$ is a collective notation for Δ_L in all layers. The PID-value distributions for protons, $f^p(\text{PID}; P)$, and for pions, $f^\pi(\text{PID}; P)$, depend on the momentum.

Given the PID-values in a sample, a PID-cut, $\text{PID}_{\text{CUT}}^p$, can be defined such that particles with $\text{PID} > \text{PID}_{\text{CUT}}^p$ are considered to be protons. The proton efficiency E^p and the pion

contamination C^π of $\text{PID}_{\text{CUT}}^p$ are defined as

$$E^p(\text{PID}_{\text{CUT}}^p; P) \equiv \int_{\text{PID}_{\text{CUT}}^p}^{\infty} f^p(\text{PID}; P) d\text{PID}, \quad (4.3)$$

$$C^\pi(\text{PID}_{\text{CUT}}^p; P) \equiv \frac{N_\pi(P)}{N_p(P)} CF^\pi(\text{PID}_{\text{CUT}}^p; P) \quad (4.4)$$

$$\equiv \frac{N_\pi(P) \int_{\text{PID}_{\text{CUT}}^p}^{\infty} f^\pi(\text{PID}; P) d\text{PID}}{N_p(P) \int_{\text{PID}_{\text{CUT}}^p}^{\infty} f^p(\text{PID}; P) d\text{PID}}, \quad (4.5)$$

with the contamination factor CF defined therein. Here $N_{p(\pi)}(P)$ is the number of true protons (pions) with momentum P , which can be estimated by solving the following equations:

$$N_p(P) = \frac{N_p|_{\text{PID} > \text{PID}'}(P)}{E^p(\text{PID}'; P)}, \quad (4.6)$$

$$N_\pi(P) = \frac{N_\pi|_{\text{PID} > \text{PID}'}(P)}{1 - E^\pi(\text{PID}'; P)}, \quad (4.7)$$

$$N(P) = N_p(P) + N_\pi(P), \quad (4.8)$$

$$N|_{\text{PID} > \text{PID}'}(P) = N_p|_{\text{PID} > \text{PID}'}(P) + N_\pi|_{\text{PID} > \text{PID}'}(P), \quad (4.9)$$

that is,

$$N_p(P) = \frac{1 - E^\pi(\text{PID}'; P) - \frac{N|_{\text{PID} > \text{PID}'}(P)}{N(P)}}{1 - E^\pi(\text{PID}'; P) - E^p(\text{PID}'; P)} N(P), \quad (4.10)$$

$$N_\pi(P) = \frac{-E^p(\text{PID}'; P) + \frac{N|_{\text{PID} > \text{PID}'}(P)}{N(P)}}{1 - E^\pi(\text{PID}'; P) - E^p(\text{PID}'; P)} N(P). \quad (4.11)$$

Here $N(P)$ is the total sample size and $\text{PID} > \text{PID}'$ is a restriction that defines a sub-sample with arbitrary PID' . Because the numbers of particles vary in different physics analyses, in this work CF rather than C is used as a criterion for particle identification.

When certain criteria are specified, e.g. $E^p \geq 99.9\%$ and $CF^\pi \leq 10^{-2}$, $\text{PID}_{\text{CUT}}^p$ can be calculated by solving Eqs. (4.3) and (4.5). In the minimum ionization region where $\beta \rightarrow 1$, no solution for $\text{PID}_{\text{CUT}}^p$ may be found due to the suppressed mass dependence of the energy loss distribution. The momentum upper bound, below which a PID cut satisfying the criteria $E^p \geq E_R^p$ and $CF^\pi \leq CF_R^\pi$ exists, is denoted as $P_{E_R^p}^{CF_R^\pi}$.

The discussion for the pion selection is analogous.

4.1.1 Computational techniques

A computational example with silicon layers is shown in Figs. 4.1-4.3.

In Fig. 4.1 the left panel shows the energy loss distribution $F_L(\Delta_L; \beta)$ calculated for a 300 μm thick silicon layer using Eqs. (3.1) – (3.6). The density correction δ in Eq. (3.4) is neglected. The Gaussian width σ is modeled as 20% Δ_p (see Section 3.1). The Landau distribution in the calculation is provided by the ROOT routine `TMath::Landau` [Ren97]. The

convolution of a Landau distribution and a Gaussian distribution (Eq. (3.6)) is calculated by evaluating the convolution integral as a Riemann sum within $\pm 5\sigma$ of the Gaussian with a step size 5 keV. The step size is fine-tuned to compromise the following contrary requirements:

- the step size should be small compared to the ranges of the energy loss spectra. The upper bound is set by MIP's (minimum ionizing particles) as about 200 keV.
- in fitting the energy loss spectra with the least-square method, the step size cannot be too small compared to the bin width (10 keV in this work), otherwise the fitting converges to non-physical results.

The right panel of Fig. 4.1 shows the corresponding calculated PID-value (PID_L) as a function of Δ_L . The momentum is fixed at 0.6 GeV/c. In calculating the PID-values, small values of F have to be regularized in order to avoid \log_{10} -divergence:

$$F \rightarrow 10^{-10}, \forall F < 10^{-10}. \quad (4.12)$$

This involves only a small amount of statistics and the effect is negligible after combining the PID-values.

Figure 4.2 shows the distributions of PID-values. In the left panel PID_L is for a single layer, while in the right panel PID is the sum of the PID-values in six identical layers. A PID-cut for protons, $\text{PID}_{\text{CUT}}^p = 1$, is also shown. The distributions for protons and pions are calculated with momentum fixed at 0.6 GeV/c. The distributions are obtained by simulating energy loss vectors, whose components uncorrelatedly follow the energy loss distributions in corresponding layers. In this work the acceptance-rejection method [Ams08] is used for the sampling.

Figure 4.3 left panel shows the momentum dependence of a PID-cut for protons with 99.9% efficiency as well as with 10^{-2} pion contamination factor. It can be read off that $P_{E_p^{99.9\%}}^{CF_{10^{-2}}^\pi} \simeq 0.75$ GeV/c, which means that in the momentum region larger than 0.75 GeV/c no PID-cut exists for a proton selection with efficiency larger than 99.9% and pion contamination factor smaller than 10^{-2} . It can also be seen from this figure, for the PID-cut shown in Fig. 4.2 ($\text{PID}_{\text{CUT}}^p = 1$ at 0.6 GeV/c), that the efficiency is 99.9% and the pion contamination factor is smaller than 10^{-2} . The right panel is the analog for the pion selection.

4.2 Results

Following the description in Section 4.1, individual PID-values are calculated from the energy loss distributions, which are extracted from real data, for the six silicon and SciFi layers (ISSD, OSSD, SFIP, SFIS, SFOP, SFOS) separately for each quadrant (Q1–4). Based on the distribution of the combined PID-values for 4 space point (4SP) tracks, the identification efficiency and contamination factor are obtained (Fig. 4.4). In addition, results for 3SP tracks are also obtained (Fig. 4.5).

The four quadrants of the Recoil Detector are separate detection systems. The particle identification performance varies among quadrants but differs significantly only in the low momentum region (Fig. 4.6).

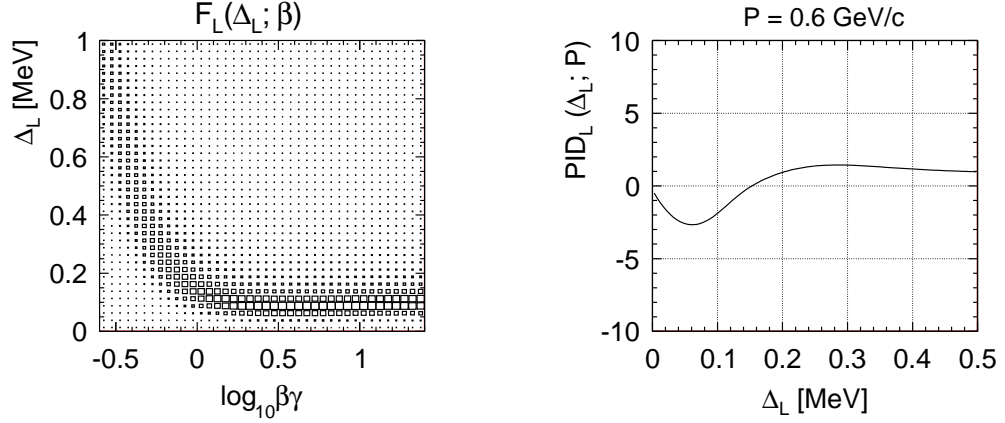


Figure 4.1: *Left*: Energy loss distribution $F_L(\Delta_L; \beta)$ calculated for a 300 μm thick silicon layer in a computational example. *Right*: the corresponding PID-value evaluated at momentum equal to 0.6 GeV/c.

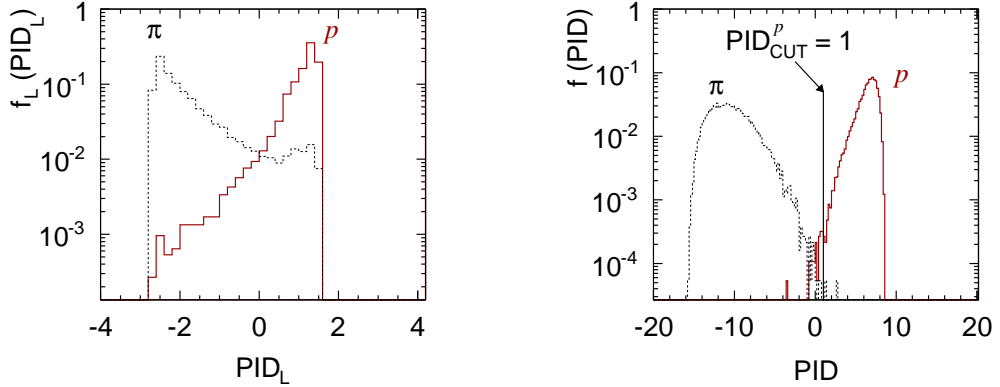


Figure 4.2: The distributions of PID-values calculated with momentum fixed at 0.6 GeV/c in the computational example. *Left*: distribution of the PID-value in one signal layer; *Right*: distribution of the sum of the PID-values in 6 identical layers. Solid red lines are for protons and dotted black lines are for pions. A PID-cut for protons, $\text{PID}_{\text{CUT}}^p = 1$, is also shown.

4.3 Comparison with conventional procedure

Conventional procedure of PID with the Recoil Detector [Lu08] is also based on the energy loss in the Recoil Detector. After the sample selection and the incident angle correction (see Sections 3.2.1 and 3.2.2), energy loss distributions are extracted separately for protons and pions in the following way. As can be seen in Fig. 3.4, protons and pions have different two-dimensional distributions in (Δ, P) where Δ is the energy loss and P is the reconstructed momentum. By selecting particles in the corresponding regions of the (Δ, P) planes in other detection layers (Fig. 4.7), the energy loss distribution functions for protons and pions in a certain layer are extracted as $F_L^{p:\Delta_L, P}$ and $F_L^{\pi:\Delta_L, P}$ in each (Δ_L, P) -bin (Fig. 4.8). The PID-value

4.3. COMPARISON WITH CONVENTIONAL PROCEDURE

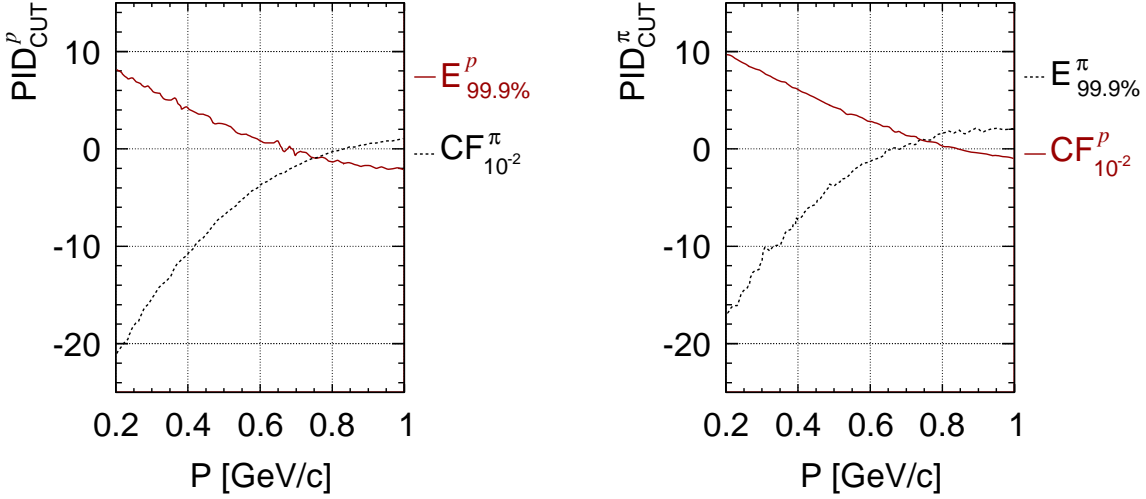


Figure 4.3: PID performance in the computational example. *Left*: PID-cut for protons (PID_{CUT}^p) with 99.9% efficiency ($E_{99.9\%}^p$) as well as with 10^{-2} pion contamination factor ($CF_{10^{-2}}^\pi$). *Right*: PID-cut for pions (PID_{CUT}^π) with 99.9% efficiency ($E_{99.9\%}^\pi$) as well as with 10^{-2} proton contamination factor ($CF_{10^{-2}}^p$).

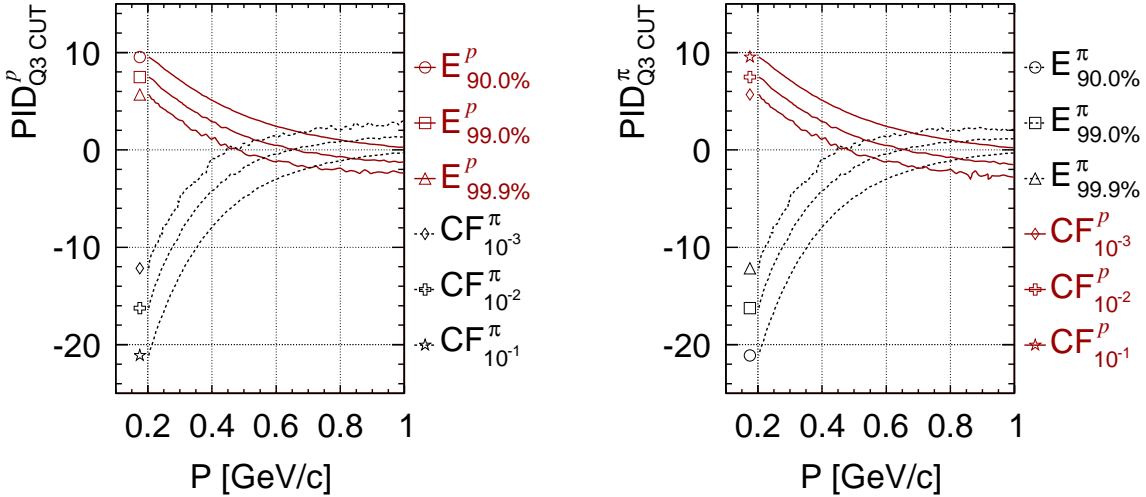


Figure 4.4: PID performance for Q3 4SP tracks. *Left*: proton selection. *Right*: pion selection.

is correspondingly calculated as (Fig. 4.9)

$$PID_L^{\Delta_L, P} = \log_{10} \frac{F_L^{p; \Delta_L, P}}{F_L^{\pi; \Delta_L, P}}, \quad PID_L^{\tilde{\Delta}, P} = \sum_L PID_L^{\Delta_L, P}. \quad (4.13)$$

In this work, several improvements have been made compared to the conventional procedure.

First, in the conventional procedure the pion sample is selected out of the positively charged particles, while the negative pion sample (simply the negatively charged particles),

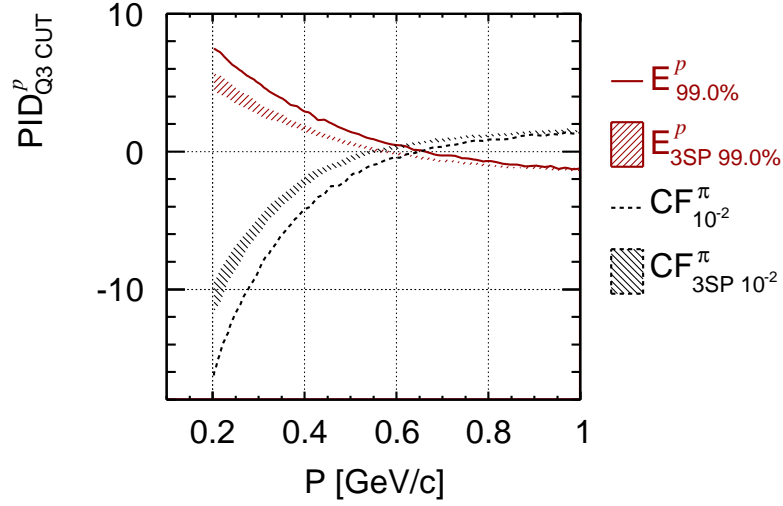


Figure 4.5: PID performance for Q3 4SP (lines) and 3SP (shaded regions) tracks. The band structure for 3SP tracks is spanned by different space point combinations.

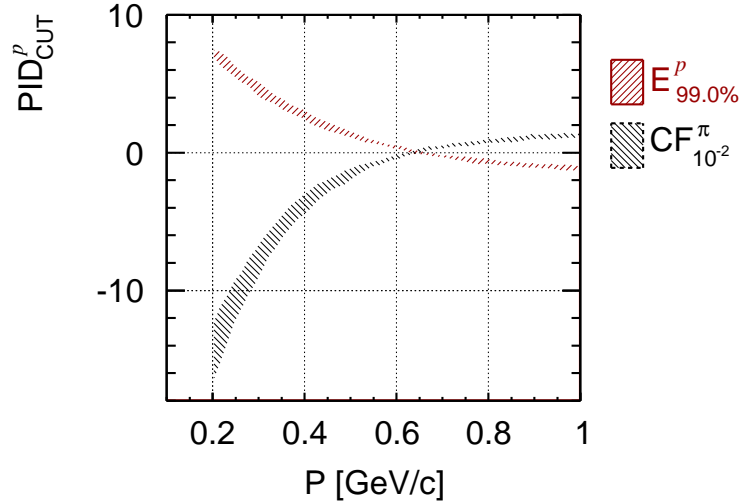


Figure 4.6: PID performance for 4SP tracks in different quadrants. The band width is spanned by the difference among quadrants.

which is cleaner and has higher statistics, is not used. Cuts in the conventional procedure have to be fine-tuned (which is sometimes difficult) in order to have enough pion statistics while keeping the sample clean.

Second, considering only the proton selection in the conventional procedure, in the high momentum region (roughly $P > 0.6$ GeV/c), the cut can not be justifiably determined because on the one hand the separation between the two types of particles is getting worse and even trends to vanish with higher momentum, on the other hand extrapolation from the low momentum region can only provide a weak constraint. In the method presented in this thesis (see Section 3.2.3), the cut to select protons in the high momentum region ($-0.2 \lesssim \log_{10} \beta\gamma \lesssim 0.15$) is interpolated between the low momentum protons and the negative pions (Fig. 3.5). A con-

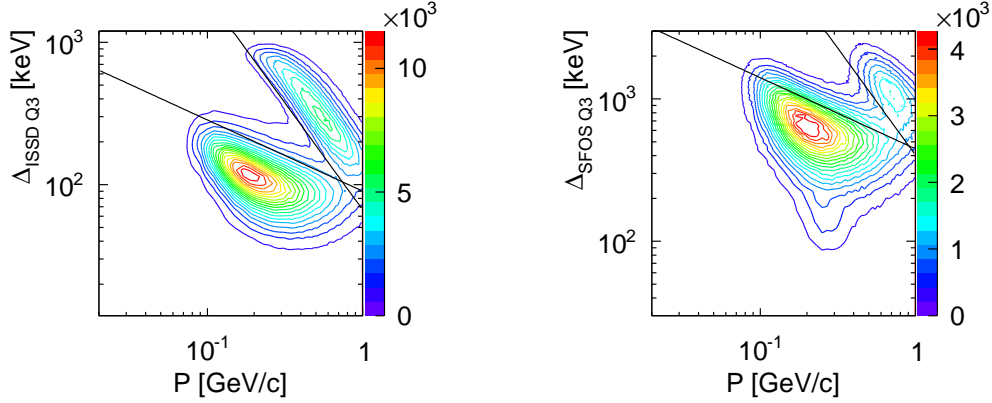


Figure 4.7: Particle selection cuts in the conventional procedure in (*left*) ISSD Q3 and (*right*) SFOS Q3. Particles in the region above both lines are selected as protons. Particles in the region below both lines are selected as pions.

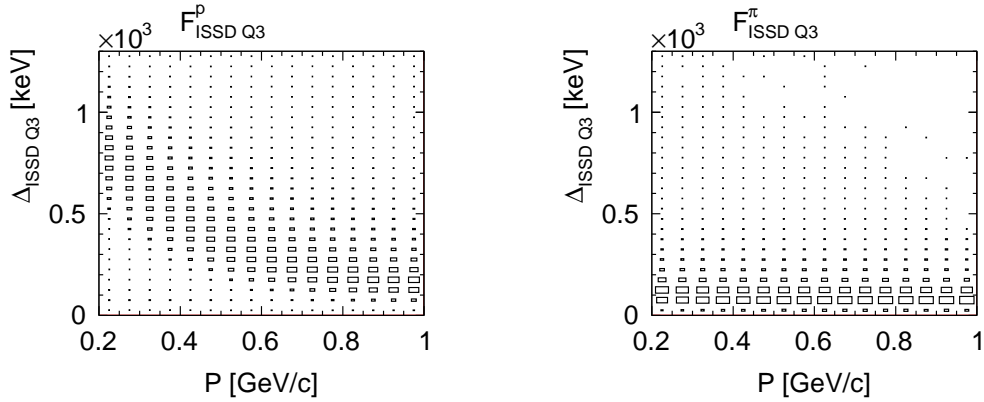


Figure 4.8: Extracted energy loss distributions in the conventional procedure in ISSD Q3 for (*left*) protons, $F_{\text{ISSD Q3}}^p$, and (*right*) pions, $F_{\text{ISSD Q3}}^\pi$.

sistent treatment for protons and pions provides a simpler and more elegant way to obtain, to understand and to apply the extracted energy loss distributions (see Chapter 5 for another application). This is the original motivation to change the momentum coordinate for a coordinate as a function solely of β ($\log_{10} \beta\gamma$ in this work).

Lastly, calculated in each (Δ_L, P) -bin, the energy loss distribution functions and the therefrom calculated PID-values in the conventional procedure suffer statistical fluctuations (see Figs. 4.8 and 4.9). Especially, the normalization of the distribution, which is the sum of all bins in Δ_L with fixed P , can not be calculated precisely in the case of low statistics. The fitting procedure in this work (see Section 3.2.4) smooths out these fluctuations. More importantly it describes the distributions in an analytic way, which enables a quantitative characterization of the PID performance¹ via Monte Carlo simulations for the extracted energy loss (see Section 4.1.1).

¹The identification efficiency provides a direct determination of the total yields for protons and pions (Eqs. (4.7) – (4.11)) which are conventionally determined by a Bayesian iteration procedure [Men97].

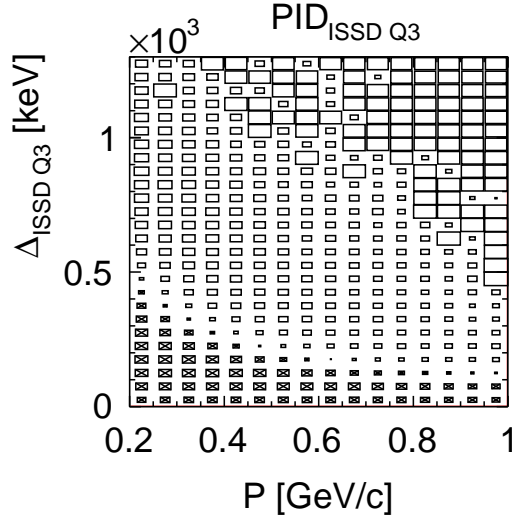


Figure 4.9: PID-value in the conventional procedure calculated from the extracted energy loss distributions in ISSD Q3. Crossed boxes are bins with negative PID-values.

4.4 Handling of special cases

In the SciFi tracker, overflow signals are set to 100 MeV [Yu09]. The background reduction in Section 3.2.3 equivalently discards all particles with such unphysically large energy loss. Therefore discussions by now have not included particles with overflow signals. The fraction of tracks with overflow signals is positively correlated to the probability for the track to have a large energy loss (Table 4.1). In an ideal case with an uniform overflow threshold, $\Delta_{\text{o.f.}}$, the

$\log_{10}\beta\gamma$	-0.5	-0.1	0.3	0.7	1.1
$\mathfrak{F}_{\text{o.f.}}$ [%]	93.2	33.0	7.8	2.2	2.9

Table 4.1: Fraction of tracks with overflow signals ($\mathfrak{F}_{\text{o.f.}}$) in different β regions, estimated from Monte Carlo simulations (see Appendix A).

fraction of tracks with overflow signals equals to the integrated probability of $F(\Delta;\beta)$ from $\Delta_{\text{o.f.}}$ to infinity. Therefore, the PID-value for an overflow signal in layer L can be defined as

$$\text{PID}_L^{\text{o.f.}}(P) \equiv \log_{10} \frac{\int_{\Delta_{\text{o.f.}}}^{\infty} F_L(\Delta; \beta\gamma = \frac{P}{m_p}) d\Delta}{\int_{\Delta_{\text{o.f.}}}^{\infty} F_L(\Delta; \beta\gamma = \frac{P}{m_\pi}) d\Delta}. \quad (4.14)$$

In the actual computation, the integration is taken from 5 MeV to 10 MeV. It is observed that the distribution of the PID-values is altered when particles with overflow signals are included. The difference is however only non-negligible for low momentum protons (Fig. 4.10).

As will be discussed in Chapter 5, the probability for a particle to be detected depends on the particle type. The PID-value for a particle with momentum P , whose energy loss is not

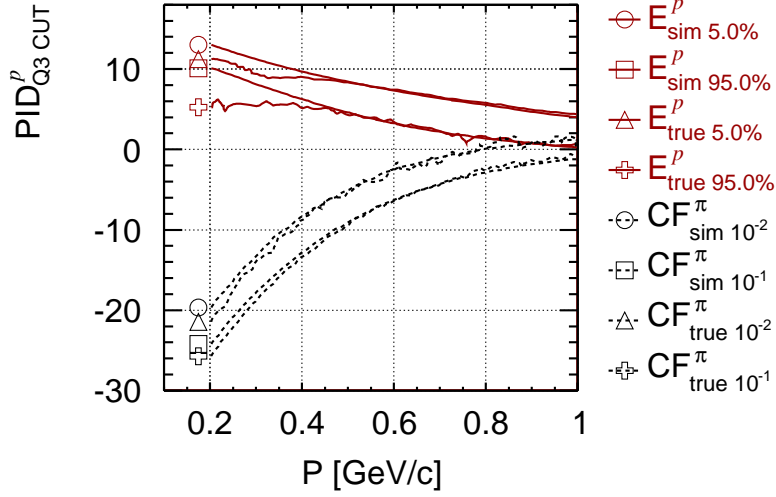


Figure 4.10: PID performance for 4SP tracks based on Monte Carlo data (see Appendix A) with [without] (true [sim]) overflow signals. The distribution of the PID-values excluding particles with overflow signals (sim) is calculated in the same way as it is done for real data; the one including them (true) is directly obtained by assigning PID-values to generated particles whose types are known.

detected by a layer L , can be defined as (undetected PID):

$$\text{PID}_L^{\text{u.d.}}(P) \equiv \log_{10} \frac{1 - \varepsilon_L(P; m_p)}{1 - \varepsilon_L(P; m_\pi)}, \quad (4.15)$$

where $\varepsilon_L(P; m)$ is the detector efficiency of layer L depending on momentum P and particle mass m . For an efficiency with a hypothetical β dependence

$$\varepsilon(\beta) = 0.895 - 0.15 \log_{10} \beta \gamma, \quad (4.16)$$

which reads $\varepsilon(\log_{10} \beta \gamma = -0.7) = 1$ and $\varepsilon(\log_{10} \beta \gamma = 1.3) = 0.7$, an undetected signal more likely belongs to a pion, and the lower the momentum is, the more unlikely a proton is undetected; therefore the undetected PID is negative over the whole momentum range and is larger in magnitude in the low momentum region, as can be seen in Fig. 4.11.

The performance of undetected PID can be estimated similarly as for normal PID-values. The difference only existing in the energy loss simulation in Section 4.1.1 is to assign an additional undetected probability (e.g. according to the extracted detector efficiency in Chapter 5) to simulate undetected signals.

With this technique the particle identification performance for 3SP tracks may be restored to the 4SP-track level (see Fig. 4.5).

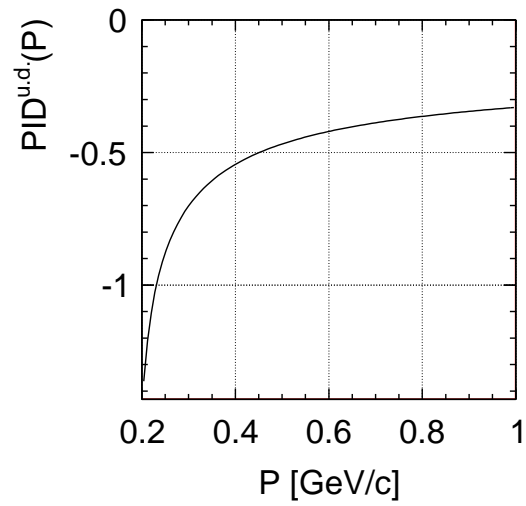


Figure 4.11: Undetection PID according to a hypothetical detector efficiency $\varepsilon(\beta) = 0.895 - 0.15 \log_{10} \beta\gamma$.

Chapter 5

Determination of detector efficiency of the scintillating fiber tracker

Given N_{all} traversing particles in the scintillating fiber (SciFi) tracker, if N_{det} of them are detected, the detector efficiency is

$$\varepsilon = \frac{N_{\text{det}}}{N_{\text{all}}}. \quad (5.1)$$

Because the scintillation light produced by the energy loss of the traversing particles is first transported by light guides and then converted into photoelectrons by photon multiplier tubes (PMTs), the overall efficiency depends on:

- the efficiency due to the fluorescence yield and the shape of the fibers $\varepsilon_{\text{scint}}$;
- the transportation efficiency of the light guides $\varepsilon_{\text{tran}}$;
- the conversion efficiency of the PMTs ε_{con} .

These efficiencies depend on the energy loss (integrated out in Eq. (5.1)) and therefore implicitly on β . Moreover, in order to suppress the noise level, only those signals are selected that are larger than a preset threshold Δ_{th} . The overall efficiency reads

$$\varepsilon(\beta) = \varepsilon_{\text{con}} \cdot \varepsilon_{\text{tran}} \cdot \varepsilon_{\text{scint}} \cdot \int_{\Delta_{\text{th}}}^{\infty} F(\Delta; \beta) d\Delta, \quad (5.2)$$

where $F(\Delta; \beta)$ is the energy loss distribution function in the SciFi tracker (see Chapter 3). In this work, the overall SciFi efficiency $\varepsilon(\beta)$ is extracted from real data using Eq. (5.1) at the fiber level.

5.1 Reconstruction of traversing particles

Tracks in the Recoil Detector are generally reconstructed from space points measured by the silicon detector and the SciFi tracker (see Chapter 2). In this work in order to separate the efficiency of the SciFi layer under investigation, the associated barrel is not used in the

tracking procedure and tracks are reconstructed only from space points in the silicon detector and the other SciFi barrel. Because of the relatively high ghost track contamination for 3SP tracks, the following requirements are placed:

- in each event, at most one track is reconstructed per quadrant;
- there is an associated signal in the photon detector (PD) A-layer.

Further, the β value of a track is calculated by mass assignment together with background reduction as described in Section 3.2.3. Here the energy loss cuts are applied in all layers involved in the tracking.

5.2 Identification of detected particles

With the reconstructed track parameters (P , θ , ϕ) (in the experiment's spherical coordinate system, see Fig. 1.2) and the measured beam position, which is taken as the track vertex, the intersection point between the track and the layer under investigation can be calculated. Figure 5.1 shows the geometry.

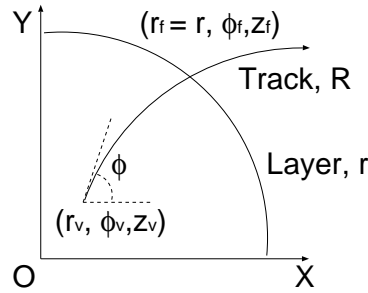


Figure 5.1: View along the z -axis of a track and a SciFi layer . The track vertex is (r_v, ϕ_v, z_v) and the intersecting point is $(r_f = r, \phi_f, z_f)$, both in cylindrical coordinate. Here r and R are the radius of the layer and the track, respectively, and ϕ is the azimuthal angle of the track momentum at the vertex.

The azimuthal angle ϕ_f of the intersecting point is calculated by solving the following equation:

$$(r \cos \phi_f - r_v \cos \phi_v - R \sin \phi)^2 + (r \sin \phi_f - r_v \sin \phi_v + R \cos \phi)^2 = R^2, \quad (5.3)$$

where r_v , r and $R[\text{m}] = P[\text{GeV}/c] \sin \theta / 0.3$ are the radius of the vertex, the layer, and the track; ϕ_v and ϕ are the azimuthal angles of the vertex and of the track momentum at the vertex, respectively. R is multiplied by -1 for negatively charged particles. Given that $r_v \sim 1$

mm, $r \sim 10$ cm and $|R| \sim 1$ m, the solution can be expanded in a series of r_v/r and r/R :

$$\begin{aligned} \phi_f = \phi + & \left\{ -\frac{1}{2} \cdot \frac{r}{R} - \frac{1}{48} \cdot \left(\frac{r}{R}\right)^3 + \mathcal{O}\left[\left(\frac{r}{R}\right)^5\right] \right\} \\ & + \left\{ -\sin(\phi - \phi_v) + \cos(\phi - \phi_v) \cdot \frac{r}{R} + \mathcal{O}\left[\left(\frac{r}{R}\right)^2\right] \right\} \frac{r_v}{r} + \mathcal{O}\left[\left(\frac{r_v}{r}\right)^2\right] \end{aligned} \quad (5.4)$$

$$= \phi - \frac{1}{2} \cdot \frac{r}{R} - \sin(\phi - \phi_v) \cdot \frac{r_v}{r} - \frac{1}{48} \cdot \left(\frac{r}{R}\right)^3 + \cos(\phi - \phi_v) \cdot \frac{r}{R} \cdot \frac{r_v}{r} + \dots \quad (5.5)$$

$$=: \sum_{i=0} \phi_i, \quad (5.6)$$

where the last line is introduced to simplify the notation with $\phi_0 = \phi$, $\phi_1 = -\frac{1}{2} \cdot \frac{r}{R}$, $\phi_2 = -\sin(\phi - \phi_v) \cdot \frac{r_v}{r}$, and so on.

The z -value of the intersecting point, z_f , is obtained via calculating the central angle ϕ_{vf} of the transverse trajectory from the vertex to the intersecting point:

$$\phi_{vf} = 2 \arcsin \left(\frac{\sqrt{(r \cos \phi_f - r_v \cos \phi_v)^2 + (r \sin \phi_f - r_v \sin \phi_v)^2}}{2R} \right), \quad (5.7)$$

$$z_f = z_v + \phi_{vf} R \cot \theta. \quad (5.8)$$

At the space point level, signals are identified with the coordinate $(\phi_{\text{Meas.}}, z_{\text{Meas.}})$. The closest space point signal to the calculated intersecting point is considered to be related to the track. The difference between the measured and the calculated coordinates in inner SFT (ISFT) Q3 is shown as a function of the reconstructed momentum in Fig. 5.2, where the azimuthal angle is calculated to different accuracies $\phi_{\text{Calc.},n^{\text{th}}} = \sum_{i=0}^n \phi_i$ (Eq. (5.6)). As can be seen from the upper panels, the deflection of a track in the magnetic field is accounted for mostly by the ϕ_1 term, while some residual effects are still seen at the low momentum region where the radius of a track is over-estimated with the initial momentum at the vertex. The reason is that in the low momentum region the momentum decrease of a particle due to the large energy loss in previous layers is significant. Comparing the plots in the upper right panel and in the middle left panel, the non-zero mean of the ϕ -difference is corrected by including the ϕ_2 term, which also narrows down the distribution. The plot for the inclusion of the ϕ_3 (ϕ_4) term in the middle right (lower left) panel shows that the additional contribution is negligible. The z -difference which is calculated with $\phi_{\text{Calc.},4^{\text{th}}}$ in the lower right plot has a non-zero mean of about 0.2 cm over the whole momentum range. If it would be due to kinematic effect, the mean of the z -difference should have been zero at the high momentum region as is the case for the ϕ -difference. Therefore this result indicates that the z -component of the vertex, z_v , may have a systematic shift with respect to the true value. Note that the geometrical resolution in ϕ and z according to the fiber diameter (1 mm) and the radius of inner SciFi (11 cm) is about 10 mrad (≈ 1 mm/11 cm) and 6 mm (≈ 1 mm/ $\sin 10^\circ$), which agrees with the widths of the distributions in the ϕ - and z -difference, respectively. In this work, the azimuthal angle of the intersecting point is calculated to the ϕ_4 term, i.e. $\phi_f = \phi_{\text{Calc.},4^{\text{th}}}$.

Because signals at the cluster level only have fiber number (Fiber No.) as identification, the hit fiber corresponding to the calculated intersecting point needs to be first located. Taking the actual alignment of the SciFi tracker into account, the hit-fiber number is looked up in the

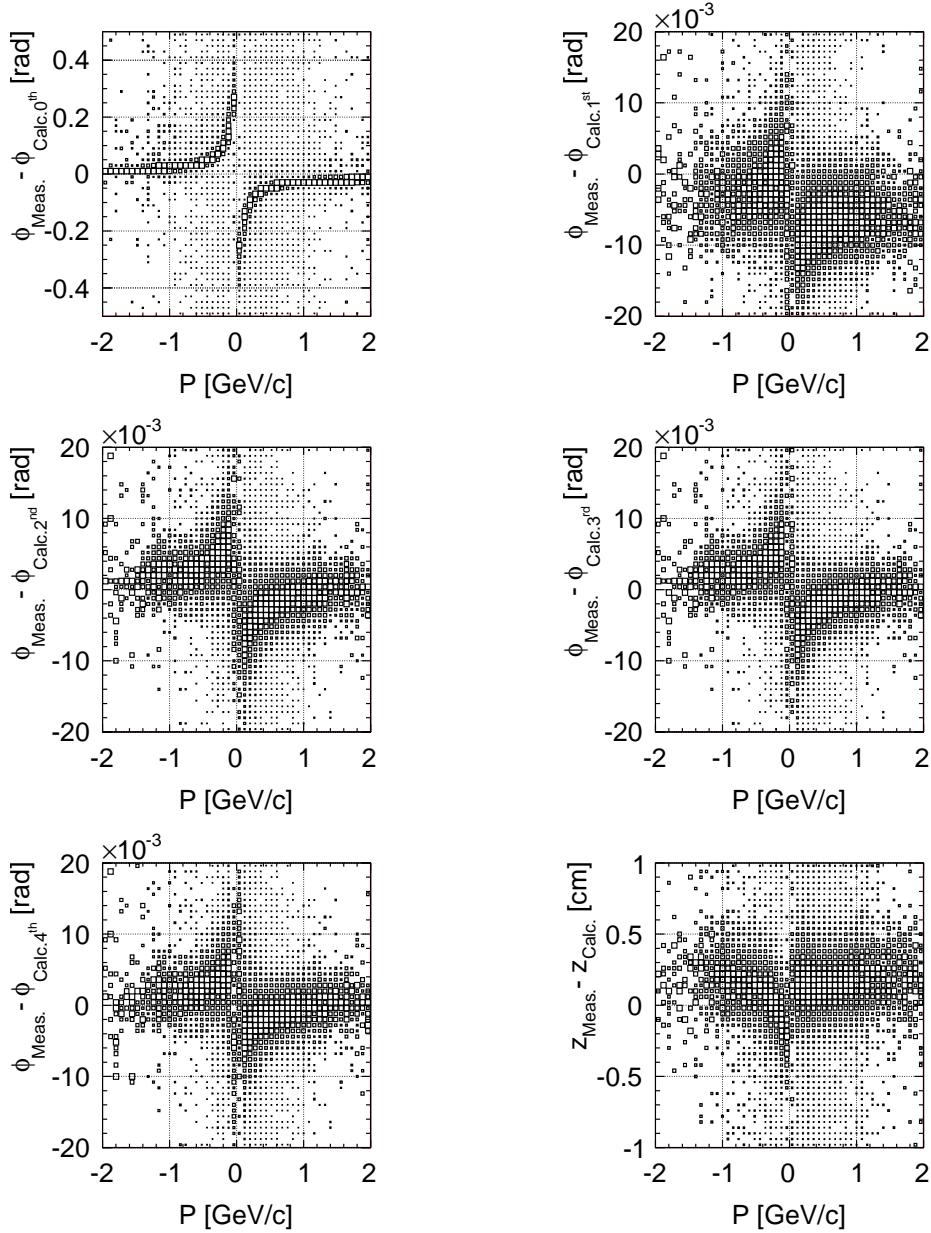


Figure 5.2: Difference between the measured and the calculated space point coordinates. Comparison is made by calculating the azimuthal angle to different accuracies: $\phi_{\text{Calc.}n^{\text{th}}} = \sum_{i=0}^n \phi_i$ (see Eq. (5.6)). The z coordinate $z_{\text{Calc.}}$ is calculate from $\phi_{\text{Calc.}4^{\text{th}}}$. A test sample for inner SciFi efficiency from real data is used, in which positive pions are not discarded and PD A-layer signals are not required (the PD A-layer signal is only critical for outer SciFi efficiency).

alignment file [Yas09] according to the calculated intersecting point. In the alignment file, the relation between fiber numbers and spatial coordinates is such that the coordinates of the grids, which are determined from different combinations between parallel and stereo fibers, are recorded: $(\phi', z'; n^p, n^s)$, where $n^{p(s)}$ is the fiber number of the parallel (stereo) fiber. Because the calculated intersecting point (ϕ_f, z_f) may not coincide with any grid, an averaged

hit-fiber number n_f is obtained in the following way. For a calculated intersecting point in a stereo layer of radius r , the closest three grids measured by $\sqrt{(r\phi' - r\phi_f)^2 + (z' - z_f)^2}$ are selected: $(\phi'_i, z'_i; n_i^s)$, $i = 1, 2, 3$. After solving the coefficients a , b and c in the linear equations:

$$n_i^s = a + bz'_i + c\phi'_i, \quad i = 1, 2, 3, \quad (5.9)$$

the hit-fiber number n_f is calculated as

$$n_f = a + bz_f + c\phi_f. \quad (5.10)$$

This exploits the fact that a cylindrical surface is locally flat. For an intersecting point in a parallel layer, only the azimuthal coordinate is considered.

Having located the hit fiber, the track is assigned to be detected if there is a measured signal in its vicinity (see below for a precise definition). Figure 5.3 upper panel shows the distributions of the differences between the measured and the calculated Fiber No. ($\delta_{\text{Fiber No.}}$) in layers SFI3 and SFOS. The wider distribution in SFOS is due to worse quality of tracking with the silicon detector and the inner SciFi (ISFT) barrel. ISFT provides a weaker constraint in track fitting due to its smaller radius. In the figure it can be seen that the measured Fiber No. distributes about the calculated one, so it is safe to define the *vicinity* as $|\delta_{\text{Fiber No.}}| \leq 10$. An exception exists when the noise level is so high that there is no way to define a window for true signals (Fig. 5.3 Lower).

Figure 5.4 shows the distribution of the fiber number difference $\delta_{\text{Fiber No.}}$ as a function of the reconstructed momentum (the momenta of negative particles are multiplied by -1). In the low momentum region of negative particles where the momentum resolution is worse, the accuracy in locating the hit fibers is limited. Therefore the following momentum requirements are applied:

- $|P| \geq 0.22$ GeV/c for negatively charged particles;
- $|P| \leq 1.49$ GeV/c for positively charged particles to avoid an overlap with negatively charged ones in the $\log_{10}\beta\gamma$ basis.

Figure 5.5 shows the distribution of $\delta_{\text{Fiber No.}}$ as a function of β after the momentum cuts. Particles with $\log_{10}\beta\gamma < 0.2$ are positively charged (mostly protons after background reduction), while those with $\log_{10}\beta\gamma > 0.2$ are negative pions. It can be read off that the uncertainty in locating the hit fiber is about 2 (6) in Fiber No. for the inner (outer) SciFi layers.

5.3 Efficiency calculation

The efficiency is calculated by counting the numbers of the traversing particles (see Section 5.1) and the detected particles (see Section 5.2), namely N_{all} and N_{det} respectively, in each (Fiber No., β)-bin with bin-width 2 (6) in Fiber No. for the inner (outer) SciFi layers:

$$\varepsilon^i = \frac{N_{\text{det}}^i}{N_{\text{all}}^i}, \quad (5.11)$$

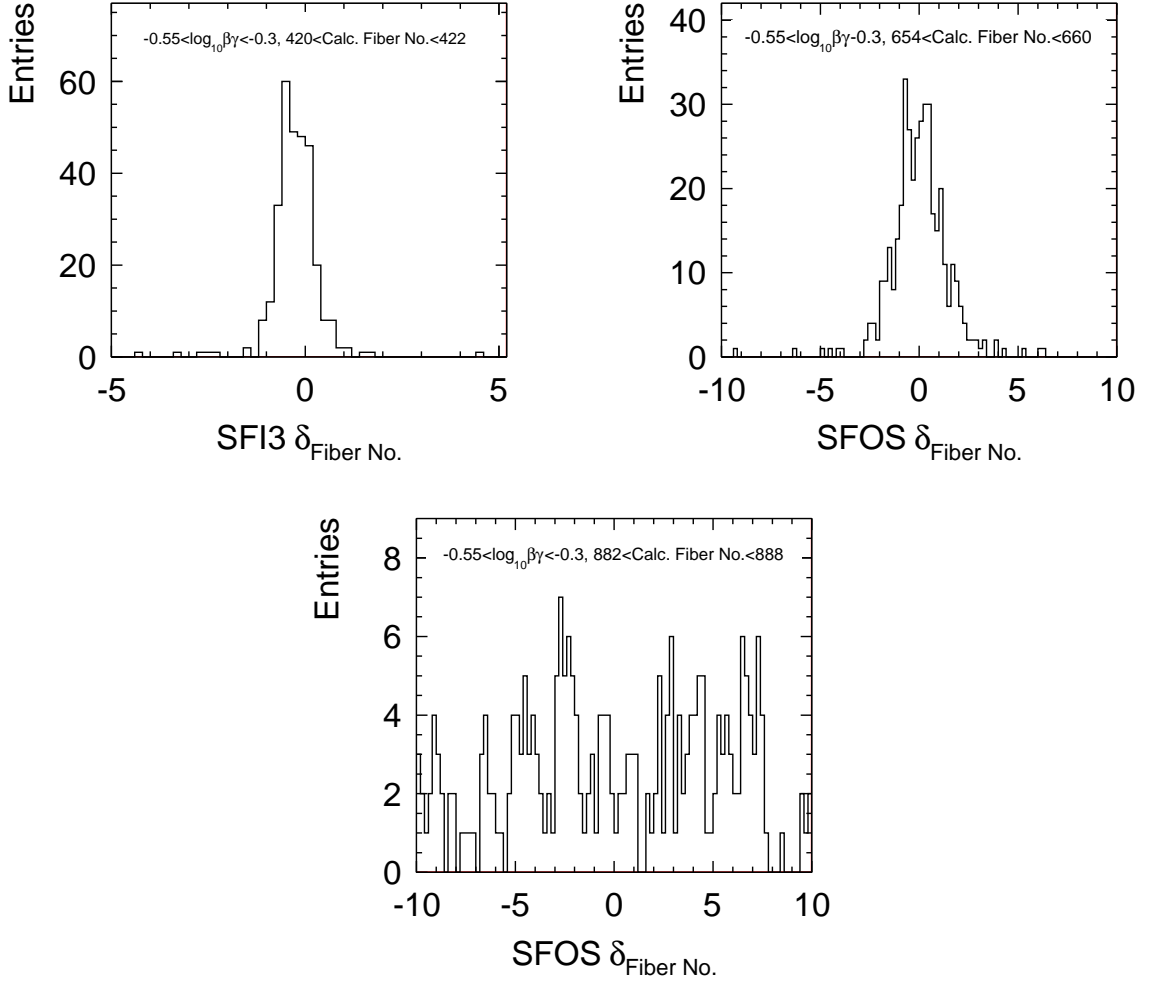


Figure 5.3: *Upper*: Distributions of the differences between the measured and the calculated fiber numbers ($\delta_{\text{Fiber No.}}$) in layers SFI3 (*left*) and SFOS (*right*). The corresponding β values and the calculated fiber numbers are shown. *Lower*: A wide distribution of $\delta_{\text{Fiber No.}}$ due to high noise level.

where i is the Fiber No.-bin index¹ ($1 \leq i \leq k$), and the β dependence is implicit. The bin-width is chosen to be slightly larger than the width of the $\delta_{\text{Fiber No.}}$ distribution. Due to the limited precision in locating the hit fiber, tracks from one bin can migrate to other bins (the *smearing effect*). Let m_i^j be the fraction of tracks migrating from bin- i to bin- j (migration from lower to upper index), while m_i^i is defined as $1 - \sum_{j \neq i} m_i^j$. The counted event numbers can be expressed as (assuming m_i^j is the same for both the traversing and the detected particle

¹Due to the cylindrical configuration of the SciFi barrels, $i = 0$ and $i = k + 1$ are understood as $i = k$ and $i = 1$, respectively.

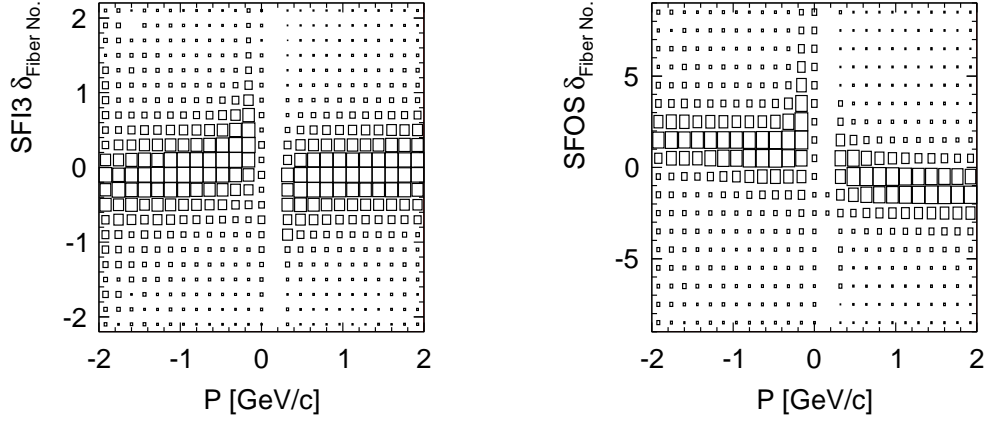


Figure 5.4: Distributions of the fiber number differences in layers (*left*) SFI3 and (*right*) SFOS as a function of the reconstructed momentum (the momenta of negative particles are multiplied by -1).

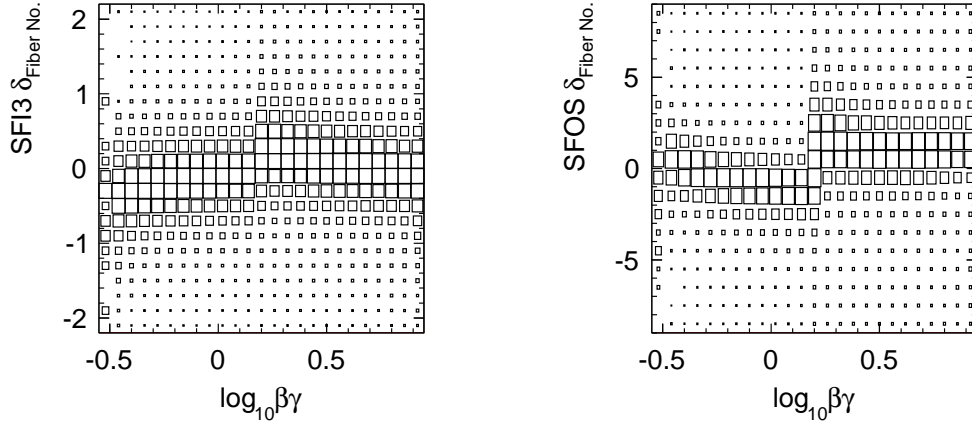


Figure 5.5: Distributions of the fiber number differences in layers (*left*) SFI3 and (*right*) SFOS as a function of β after the momentum cuts.

samples):

$$N_{\text{all}}^i = \sum_{j=1}^k m_j^i \tilde{N}_{\text{all}}^j, \quad (5.12)$$

$$N_{\text{det}}^i = \sum_{j=1}^k m_j^i \tilde{N}_{\text{det}}^j = \sum_{j=1}^k m_j^i \tilde{N}_{\text{all}}^j \tilde{\varepsilon}^j, \quad (5.13)$$

where quantities with $\tilde{}$ are the corresponding true ones without the smearing effect, and $\tilde{\varepsilon} = \tilde{N}_{\text{det}}/\tilde{N}_{\text{all}}$ is the true efficiency. Equations (5.12) and (5.13) can be rewritten in a matrix

form:

$$\begin{pmatrix} N_{\text{all}}^1 \\ N_{\text{all}}^2 \\ \vdots \\ N_{\text{all}}^k \end{pmatrix} = \underline{\underline{M}} \begin{pmatrix} \tilde{N}_{\text{all}}^1 \\ \tilde{N}_{\text{all}}^2 \\ \vdots \\ \tilde{N}_{\text{all}}^k \end{pmatrix}, \quad \begin{pmatrix} N_{\text{det}}^1 \\ N_{\text{det}}^2 \\ \vdots \\ N_{\text{det}}^k \end{pmatrix} = \underline{\underline{M}} \begin{pmatrix} \tilde{N}_{\text{det}}^1 \\ \tilde{N}_{\text{det}}^2 \\ \vdots \\ \tilde{N}_{\text{det}}^k \end{pmatrix} = \underline{\underline{M}} \begin{pmatrix} \tilde{N}_{\text{all}}^1 \tilde{\varepsilon}^1 \\ \tilde{N}_{\text{all}}^2 \tilde{\varepsilon}^2 \\ \vdots \\ \tilde{N}_{\text{all}}^k \tilde{\varepsilon}^k \end{pmatrix}, \quad (5.14)$$

where $\underline{\underline{M}}$ is called the smearing matrix with its element at the i^{th} -row j^{th} -column $[\underline{\underline{M}}]_{ij} = m_j^i$ (upper row, lower column). The leading contribution to the smearing effect is the migration between neighboring bins, for which $\underline{\underline{M}}$ is of a quasi-diagonal form:

$$\underline{\underline{M}} = \begin{pmatrix} m_1^1 & m_2^1 & 0 & \dots & 0 & m_k^1 \\ m_1^2 & m_2^2 & m_3^2 & 0 & \dots & 0 \\ & & & \ddots & & \\ 0 & \dots & 0 & m_{k-2}^{k-1} & m_{k-1}^{k-1} & m_k^{k-1} \\ m_1^k & 0 & \dots & 0 & m_{k-1}^k & m_k^k \end{pmatrix}, \quad (5.15)$$

where $m_j^i = 0$ for $2 \leq |i - j| \leq k - 2$.

In principle, the true efficiencies $\tilde{\varepsilon}^i$ can be calculated using pre-determined migration fractions m_j^i . Alternatively, it is noticed that m_j^i decreases with increasing bin-width. In the limit $m_j^i \rightarrow 0$, equation (5.14) reduces to $N_{\text{det}}^i / N_{\text{all}}^i \rightarrow \tilde{\varepsilon}^i$, however, at the cost of a finer resolution. On the other hand, if $\tilde{\varepsilon}^i$ is homogeneous over bins, namely $\tilde{\varepsilon}^1 \simeq \tilde{\varepsilon}^2 \simeq \dots \simeq \tilde{\varepsilon}^k$, then Eq. (5.14) also reduces to $N_{\text{det}}^i / N_{\text{all}}^i \simeq \tilde{\varepsilon}^i$. In either of the latter cases, equation (5.11) is justified without the exact knowledge of the migration fractions.

In this work, the smearing matrix $\underline{\underline{M}}$ and its inverse $\underline{\underline{W}}$ are directly constructed from the detected sample. For each detected particle, the hit-fiber number is calculated and related to the measured signal. The distribution in Fiber No. of the measured signals is $N_{\text{det, Meas.}}^i = \tilde{N}_{\text{det}}^i$. The distribution of the detected particles in the calculated and measured fiber numbers is shown in Fig. 5.6. The non-zero entries off the diagonal line are due to the smearing effect.

Let n_j^i denote the number of detected particles in bin- j of the calculated fiber number and bin- i of the measured fiber number (upper calculated, lower measured). The elements of $\underline{\underline{M}}$ and $\underline{\underline{W}}$ are²

$$[\underline{\underline{M}}]_{ij} = \frac{n_j^i}{\sum_k n_k^j}, \quad (5.16)$$

$$[\underline{\underline{W}}]_{ij} = \frac{n_i^j}{\sum_k n_k^j}. \quad (5.17)$$

²In general $\underline{\underline{M}}$ may not have an inverse. The matrix $\underline{\underline{W}}$ constructed in this way may not fulfill the definition of an inverse matrix: $\underline{\underline{M}} \underline{\underline{W}} = \underline{\underline{W}} \underline{\underline{M}} = \underline{\underline{1}}$. Nevertheless, the inversion of the smearing matrix should be understood in a transformation point of view, that is, it transforms a calculated distribution back to the true (i.e. measured or *unfolded*) distribution, i.e. $\underline{\tilde{N}} = \underline{\underline{W}} \underline{N}$ where \underline{N} ($\underline{\tilde{N}}$) is the vector consisting of the calculated (true) distribution, whereas $\underline{N} = \underline{\underline{M}} \underline{\tilde{N}}$.

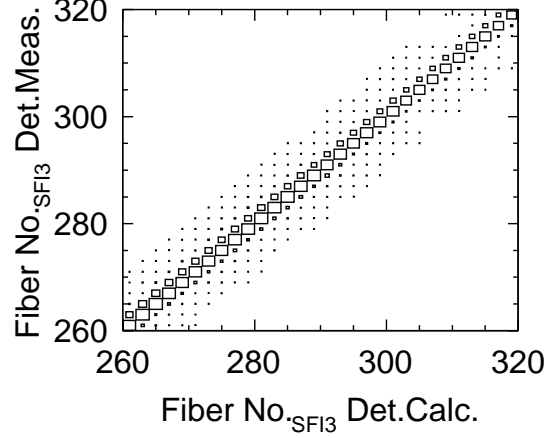


Figure 5.6: Distribution of the detected particles in the calculated fiber number (Fiber No. Det.Calc.) and the measured fiber number (Fiber No. Det.Meas.). Non-zero entries off the diagonal line are due to the smearing effect. Because of the cut $|\delta_{\text{Fiber No.}} \equiv \text{Fiber No. Det.Calc.} - \text{Fiber No. Det.Meas.}| \leq 10$ (Section 5.2), entries far off the diagonal line are null. Real data with $-0.3 \leq \log_{10} \beta\gamma \leq -0.05$ are used.

The unfolded distribution of the traversing particles $N_{\text{all,Unf.}}^i = \tilde{N}_{\text{all}}^i$ is then calculated as

$$\begin{pmatrix} N_{\text{all,Unf.}}^1 \\ N_{\text{all,Unf.}}^2 \\ \vdots \\ N_{\text{all,Unf.}}^k \end{pmatrix} = \underline{\underline{W}} \begin{pmatrix} N_{\text{all}}^1 \\ N_{\text{all}}^2 \\ \vdots \\ N_{\text{all}}^k \end{pmatrix}, \quad (5.18)$$

and is shown in Fig. 5.7 (*left panel*). Comparison between the calculated efficiency,

$$\varepsilon_{\text{Calc.}} = \frac{N_{\text{det}}}{N_{\text{all}}}, \quad (5.19)$$

and the unfolded one,

$$\varepsilon_{\text{Unf.}} \equiv \frac{N_{\text{det,Meas.}}}{N_{\text{all,Unf.}}}, \quad (5.20)$$

is shown in Fig. 5.7 (*right panel*). As can be seen, the difference after the unfolding is small for the involved fibers in the selected kinematic region $-0.3 \leq \log_{10} \beta\gamma \leq -0.05$. This is explained by the homogeneity of the efficiency over the Fiber No.-bins.

In this work, Eq. (5.19) is used for the final calculations. The difference between the calculated and unfolded efficiencies is assigned as a systematic error:

$$\delta_{\text{sys.}} = |\varepsilon_{\text{Unf.}} - \varepsilon_{\text{Calc.}}|. \quad (5.21)$$

The statistical error of the efficiency is determined according to the binomial distribution [Ams08]: given N_{all} particles, the probability for a particle to be detected is ε , the probability

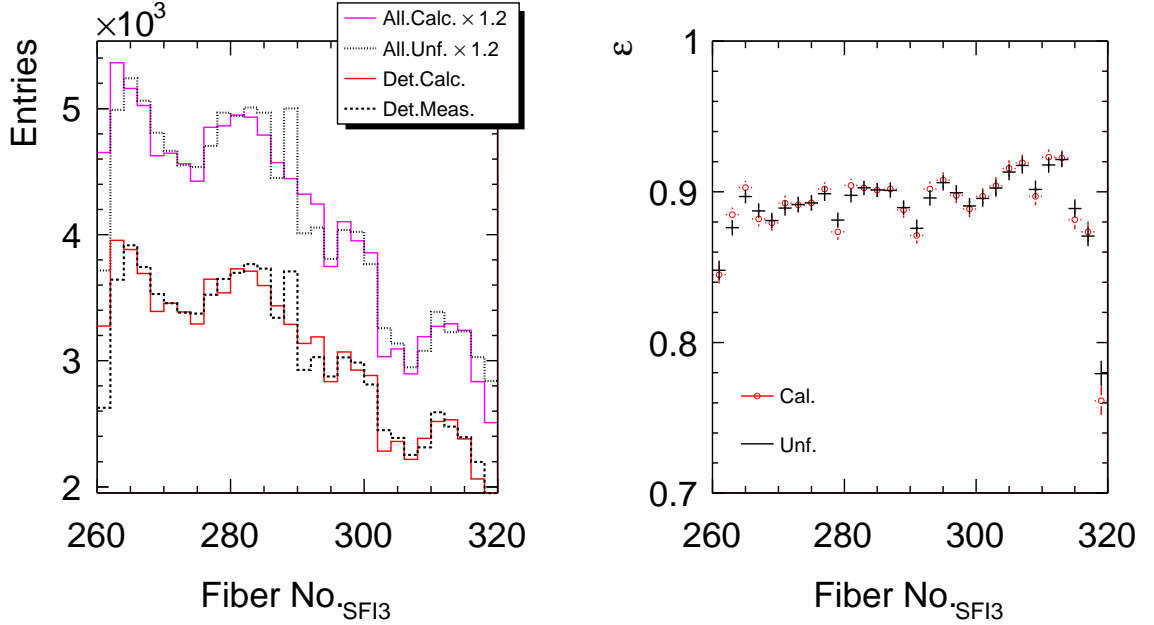


Figure 5.7: *Left*: unfolded distribution of the traversing particles (dotted black curve). For comparison, the calculated distribution of the traversing particle (solid magenta curve), the measured distribution of the detected particle (dashed black curve), and the calculated distribution of the detected particles (solid red curve) are shown. For illustration purpose, the distributions of the traversing samples are scaled by a factor of 1.2. *Right*: comparison between the calculated (red circle) and the unfolded (black point) efficiencies. The difference is small because of the homogeneity of the efficiency over the bins. Real data with $-0.3 \leq \log_{10} \beta\gamma \leq -0.05$ are used.

that N_{det} particles are detected is $\frac{N_{\text{all}}!}{N_{\text{det}}!(N_{\text{all}}-N_{\text{det}})!} \varepsilon^{N_{\text{det}}} (1-\varepsilon)^{N_{\text{all}}-N_{\text{det}}}$, and the error of N_{det} is

$$\delta N_{\text{det}} = \sqrt{N_{\text{all}} \varepsilon (1-\varepsilon)}, \quad (5.22)$$

which leads to the error of ε :

$$\delta_{\text{stat.}} = \frac{\delta N_{\text{det}}}{N_{\text{all}}} = \sqrt{\frac{\varepsilon(1-\varepsilon)}{N_{\text{all}}}}. \quad (5.23)$$

5.4 Results

(Plots in this section are shown in gray scale. For plots in color scale, see Appendix B.)

Figure 5.8 shows the distributions of the reconstructed traversing particles (see Section 5.1) in β and Fiber No.. Fiber numbers from large to small correspond to quadrant (Q) 2, 1, 4 and 3. Bins with low/no statistics are marked with blanks. The periodical blanks are due to the passive holding structure of the silicon detector. The low statistics in inner SciFi (SF11-4) Q2 with fiber numbers about 550-600 is due to problematic fibers in the corresponding part of SFOS, see discussions below. On the other hand, because of the low pion efficiency

of the silicon detector Q1 [Mus09], the highest β bins in the SciFi tracker Q1 are also of low statistics. Figure 5.9 shows the distributions of the detected particles (see Section 5.2), from which the distribution of $\delta_{\text{Fiber No.}}$ in each (Fiber No., β)-bin is extracted (like the ones in Fig. 5.3). The root mean square (RMS) and the mean values of these distributions are shown in Figs. 5.10 and 5.11. In SFI3, SFI4, SFOP, SFOS there are regions with very large RMS's. Further study shows that this is most likely due to bad PMTs in SFOP and SFOS. The RMS and mean values of $\delta_{\text{Fiber No.}}$ in each (Fiber No., β)-bin are good indicators of the quality of locating hit fibers.

The efficiencies are then calculated in each (Fiber No., β)-bin according to Eq. (5.11) (see Section 5.3). Results are shown in Fig. 5.12 and the statistical errors are shown in Fig. 5.13. The inner SciFi layers are determined to have efficiencies of about 90% (80%) in the low (high) β region. The difference between the efficiencies of the inner and outer SciFi layers is due to the different layer configurations (Fig. 2.4 *right* panel). The SFOP and SFOS layers each consists of two layers of fibers. Therefore the efficiency of SFOP and SFOS is about $\left[1 - (1 - 90\%)^2\right] \simeq 99\%$ ($\left[1 - (1 - 80\%)^2\right] \simeq 96\%$) in the low (high) β region, which is confirmed by the results in the bottom panel of Fig. 5.12. The discontinuity between the efficiencies for protons ($\log_{10}\beta\gamma < 0.2$) and pions ($\log_{10}\beta\gamma > 0.2$) indicates that certain effects besides energy loss (see Eq. (5.2)) contribute to the detector efficiency. One possible source may be the different ghost track contamination for the selected proton and pion samples. The proton has a momentum of about 1.5 GeV/c at $\log_{10}\beta\gamma = 0.2$, where the pion has a momentum of about 0.2 GeV/c. The ghost track contamination for pions is higher because of the worse tracking quality at the low momentum region. This leads to an over-estimated number of traversing particles (N_{all}) and therefore an under-estimated efficiency for the pion in its first $\log_{10}\beta\gamma$ -bins. This also explains the rising trend of the efficiency with increasing β in $\log_{10}\beta\gamma > 0.2$, which is not expected from the energy loss point of view.

From the systematic error in Fig. 5.14, which is defined as the difference between the unfolded and calculated efficiencies, it can be concluded that the smearing effect is negligible compared to the statistical error.

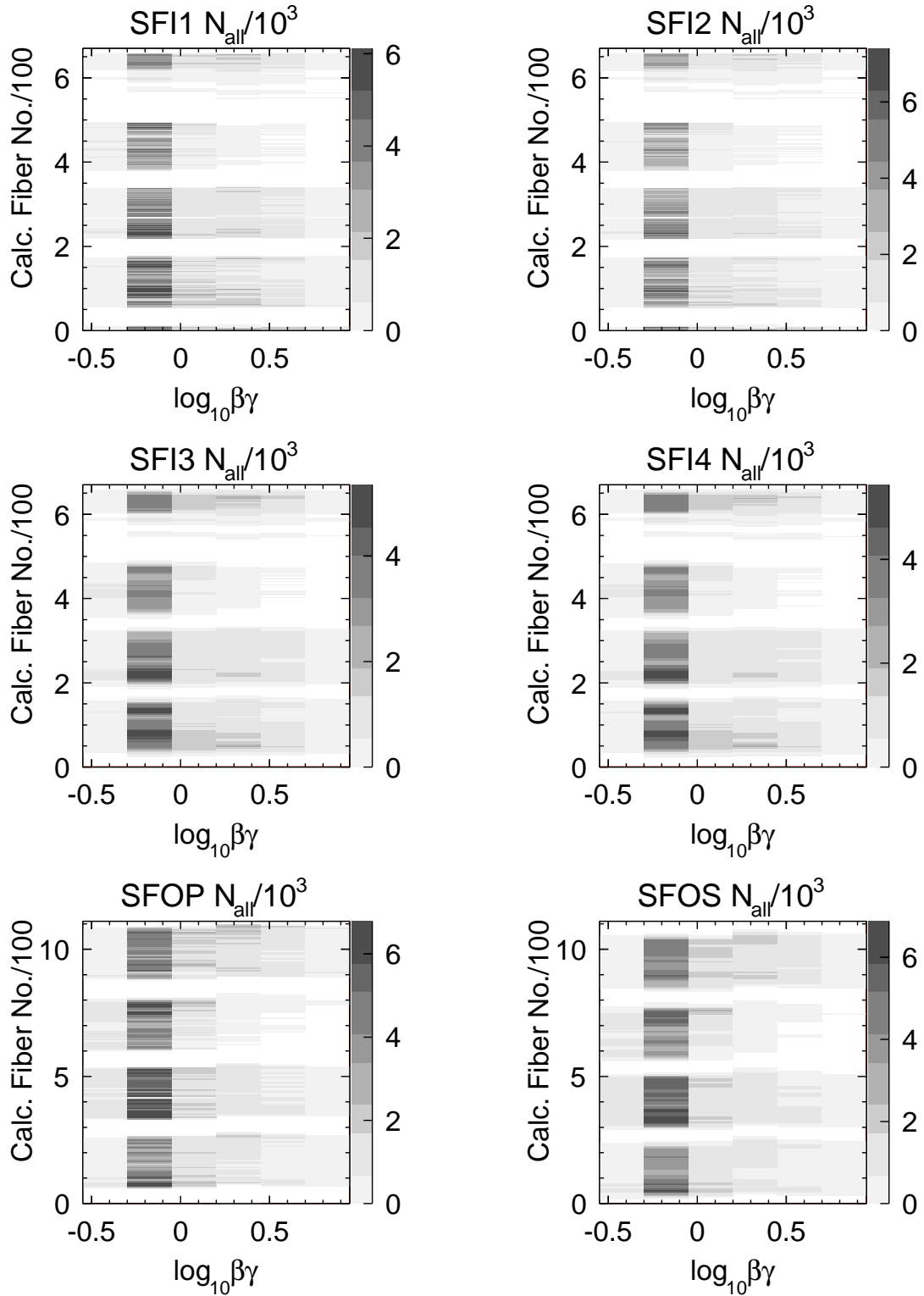
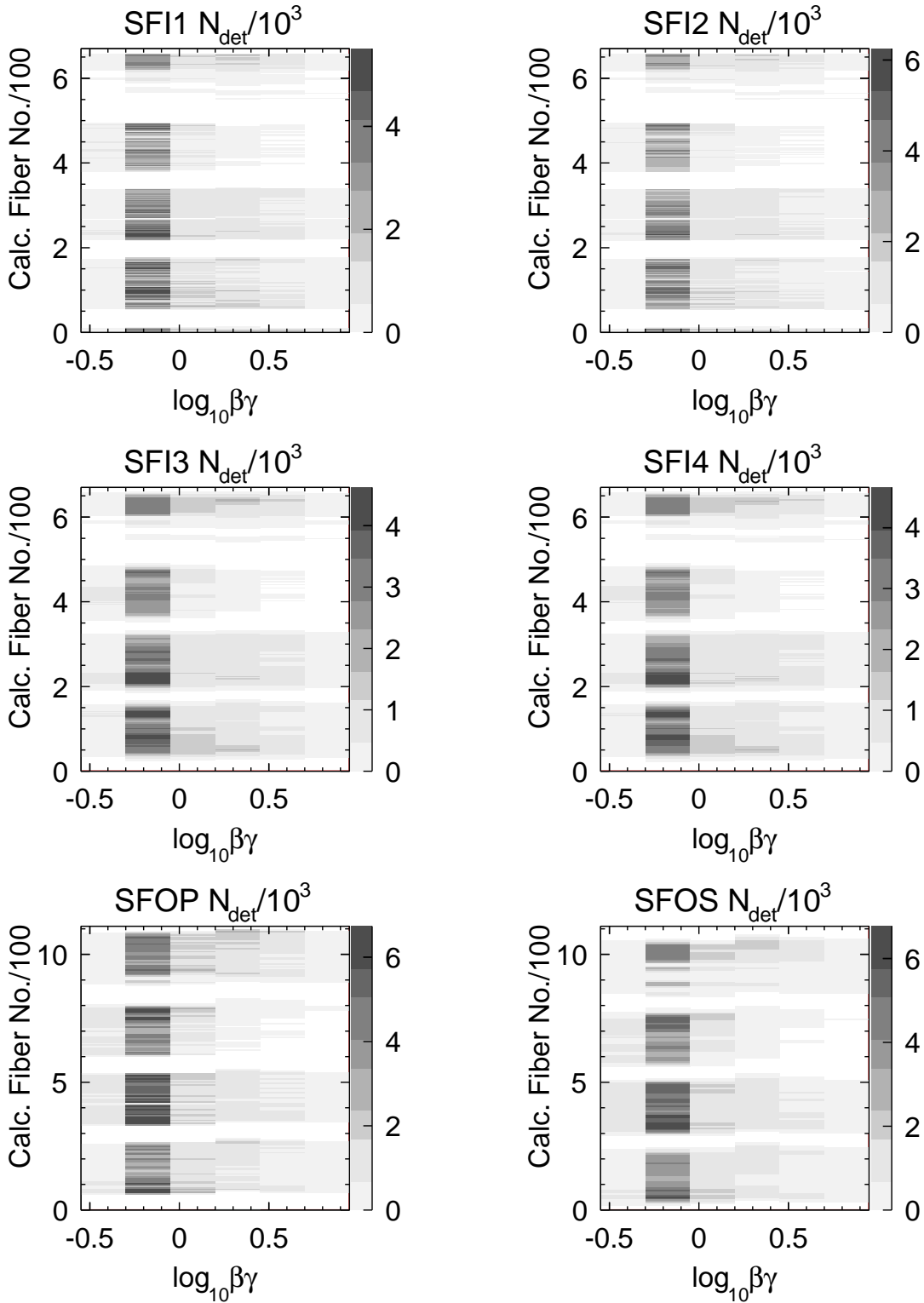


Figure 5.8: Distributions of the reconstructed traversing particles in β and the calculated Fiber No.. Fiber numbers from large to small correspond to quadrant (Q) 2, 1, 4 and 3.

Figure 5.9: Distributions of the detected particles in β and the calculated Fiber No..

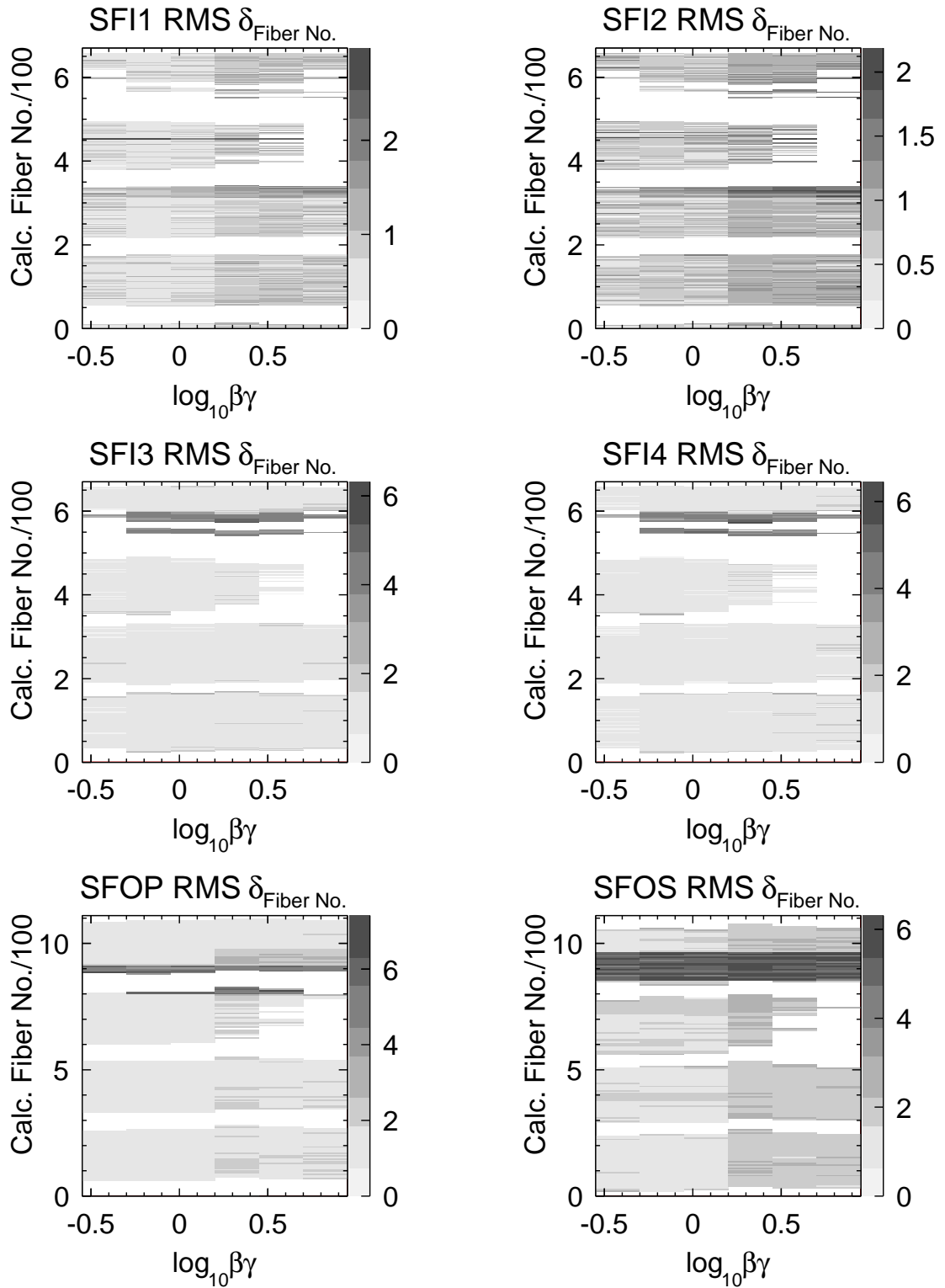


Figure 5.10: Root mean square (RMS) of the fiber number difference in each (Fiber No., β)-bin.

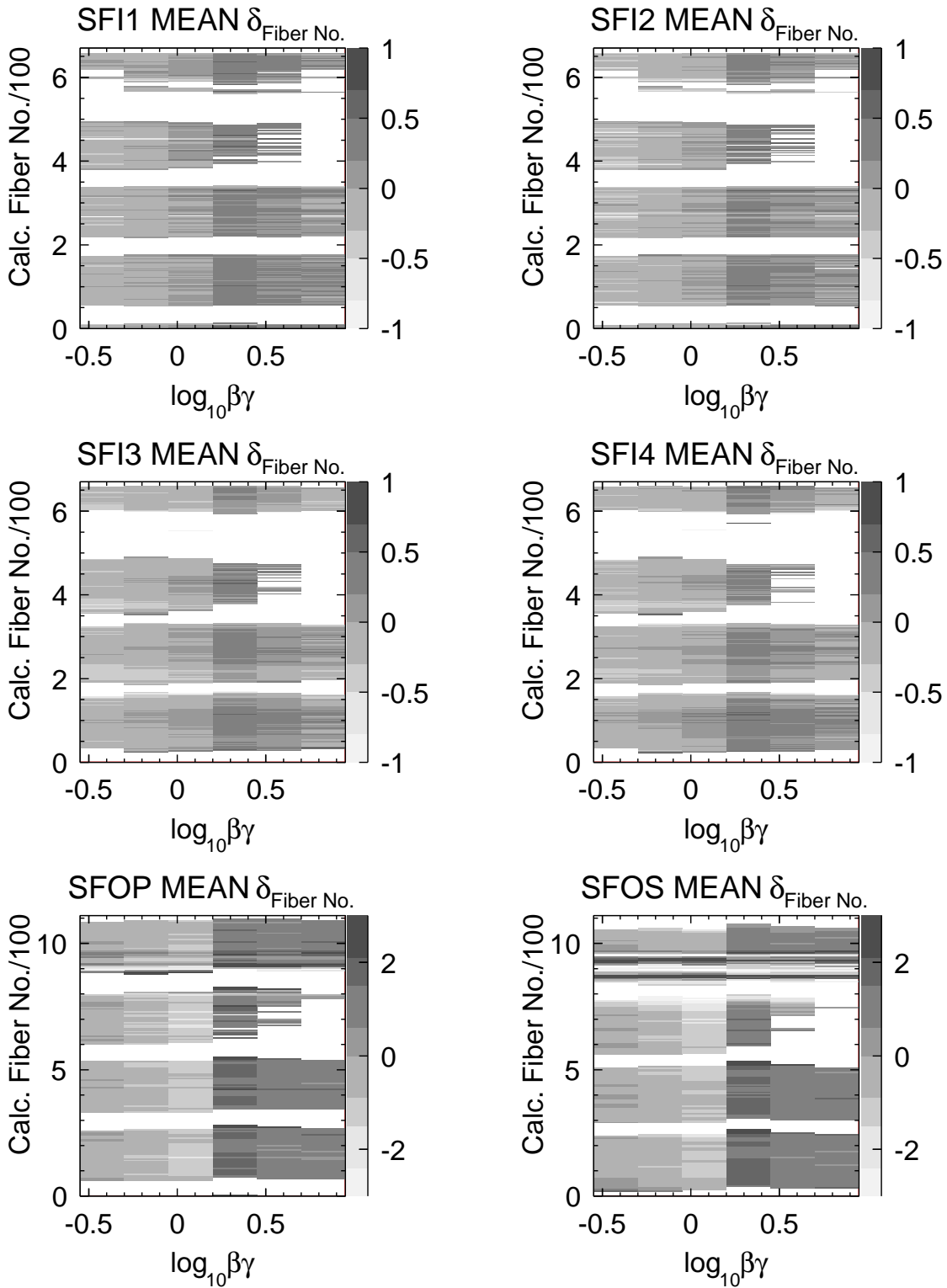


Figure 5.11: Mean value of the fiber number difference in each (Fiber No., β)-bin.

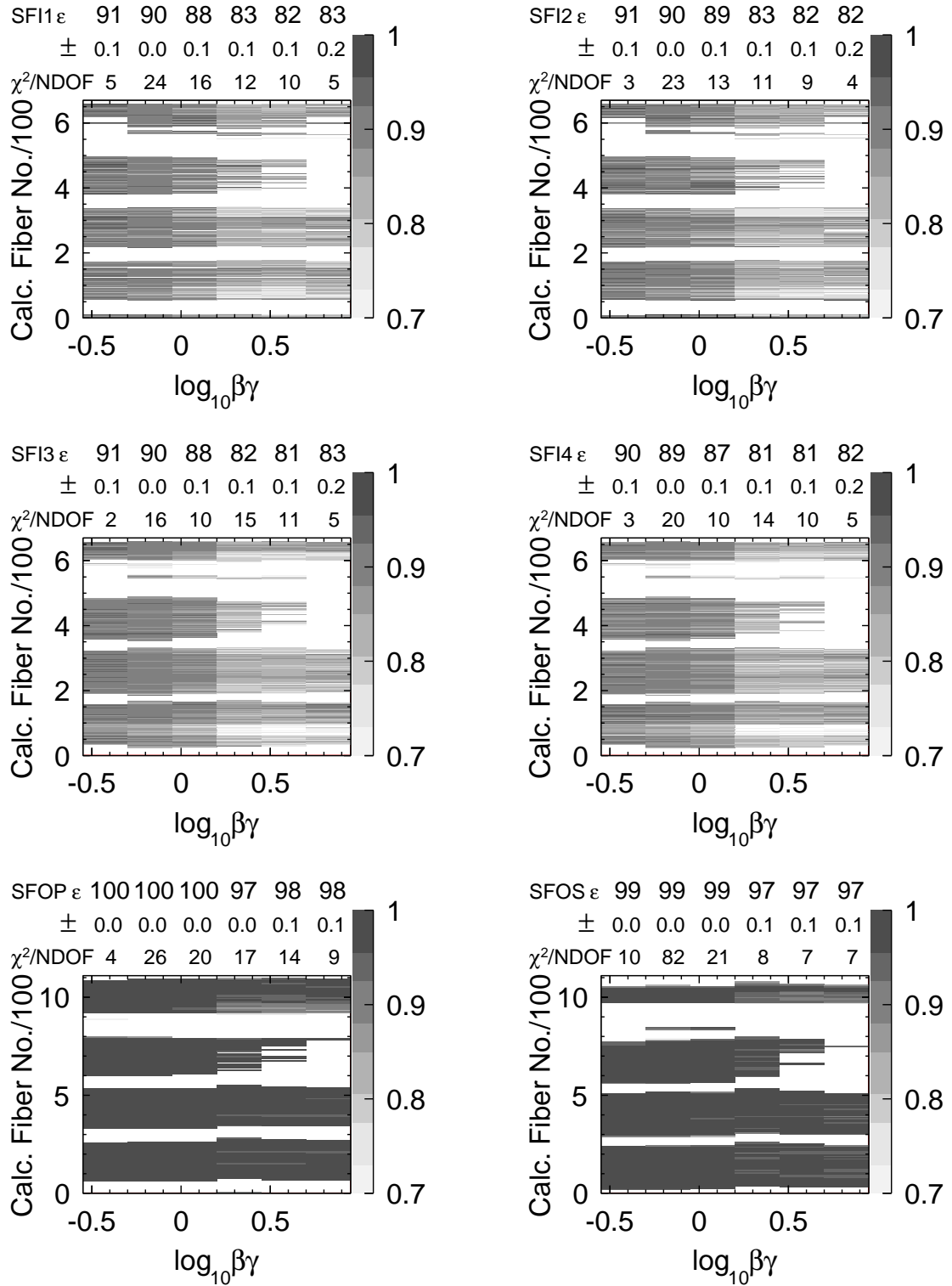


Figure 5.12: Detector efficiencies of the SciFi layers. In each $\log_{10}\beta\gamma$ -bin all efficiencies above 60%/80% (for inner/outer SciFi) are fitted to a constant function. The results are shown in the table which is aligned to the corresponding $\log_{10}\beta\gamma$ -bins in the plot (*upper line*: fitted efficiency; *middle*: fitting error; *lower*: χ^2/NDOF). Fitted efficiency and its error are in percentage.

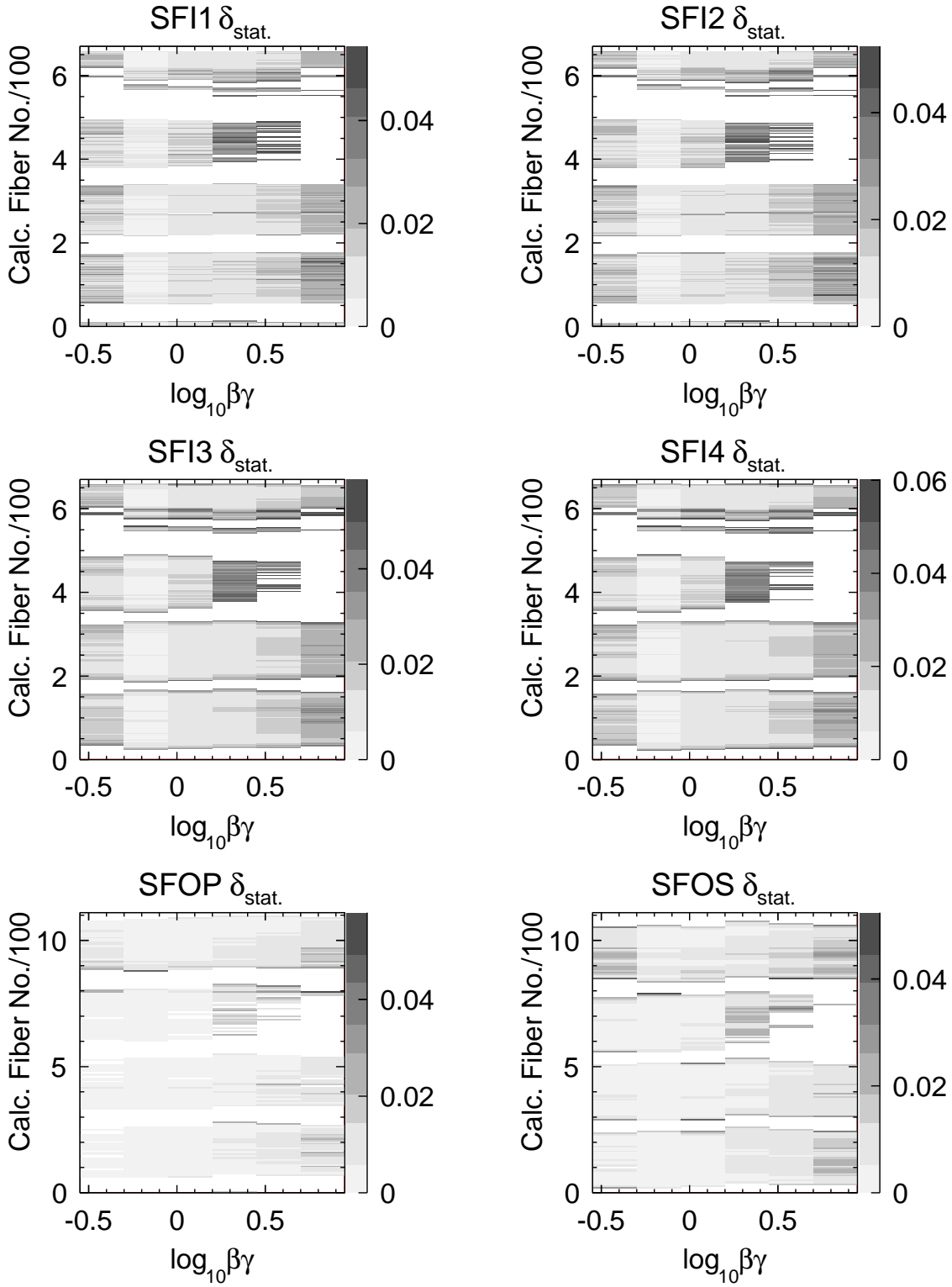


Figure 5.13: Statistical errors of detector efficiencies of the SciFi layers.

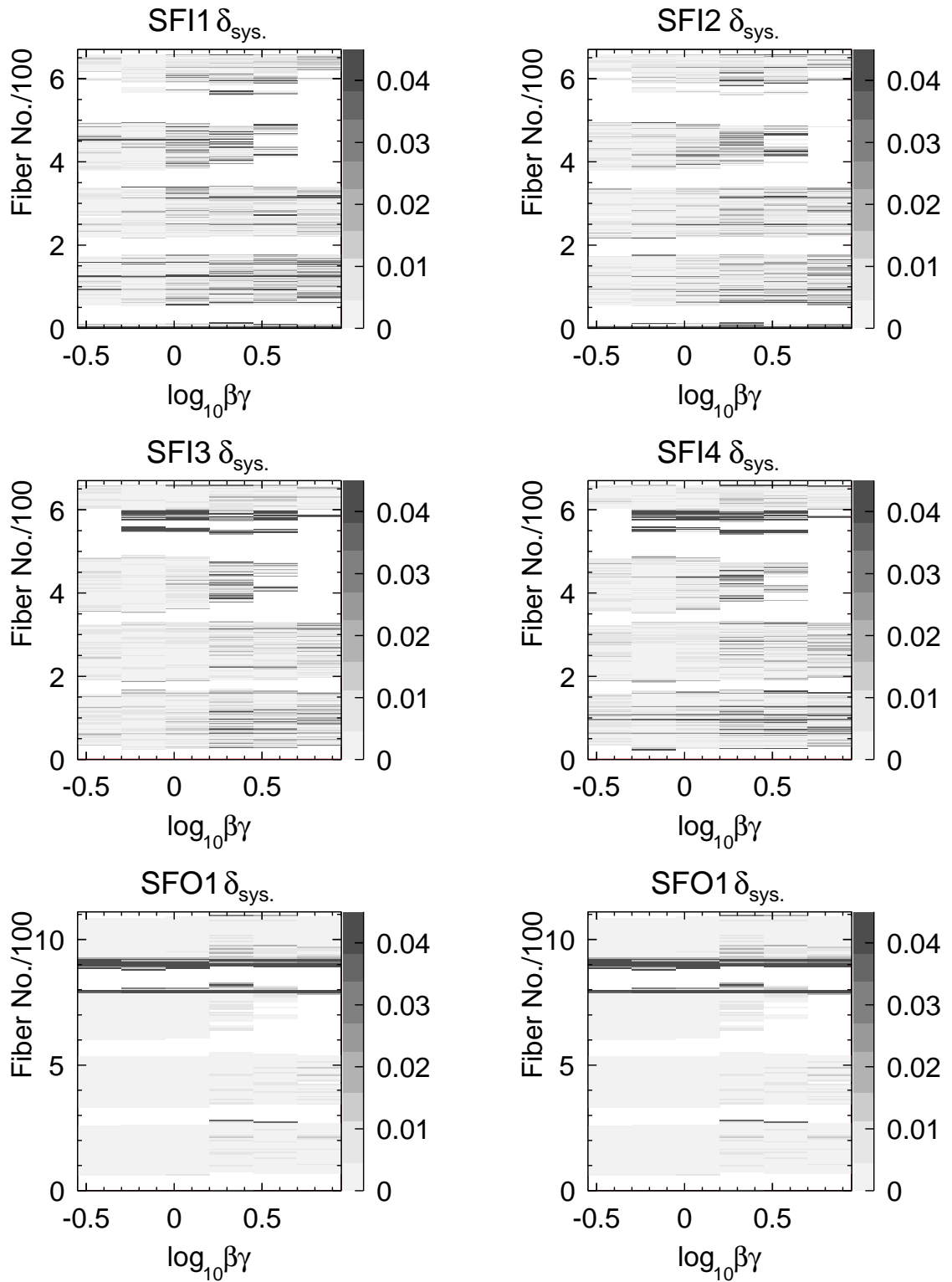


Figure 5.14: Systematic errors of detector efficiencies of the SciFi layers.

Chapter 6

Summary and conclusion

With the Recoil Detector, HERMES is able to measure precisely deeply virtual Compton scattering (DVCS), which provides access to the angular momenta of partons in the nucleon. In order to detect the recoiling proton and to identify the background, particle identification needs to be developed. In this work, a systematic procedure for particle identification (PID) with the Recoil Detector using energy loss is developed, which allows for determination of the PID efficiency and contamination (Section 4.1). The Recoil Detector with this procedure enables proton identification with 99% efficiency and 10^{-2} pion contamination¹ up to a momentum of about 0.6 GeV/c, and with 90% efficiency and 10^{-1} pion contamination up to about 1 GeV/c (Section 4.2).

Specifically, the energy loss distribution is extracted from real data via (Section 3.2.3)

- mass assignment followed by
- background reduction.

The PID-value, defined as the relative probability for a particle with certain momentum and energy loss to be a proton rather than a pion, is generated in

- Monte Carlo simulations for energy loss in each detection layer (Section 4.1.1).

The simulation is possible because the distribution functions are analytically known; this is achieved by

- physics-motivated fits to the energy loss vs. velocity spectra (Section 3.2.4).

This Monte Carlo technique enables a direct calculation for the PID efficiency and contamination (Section 4.1.1).

Several improvements, like a consistent treatment of protons and pions in extracting the energy loss distribution, have been made in this work compared to the conventional PID procedure (Section 4.3). Special cases — the overflow signals in the scintillating fiber tracker and undetected signals — are handled (Section 4.4).

The detector efficiency of the scintillating fiber tracker of the Recoil Detector is determined in this work. Traversing particles are first reconstructed by special tracking with tracking quality cuts (Section 5.1). The detected particles are identified out of the traversing particles via

¹To be understood as contamination factor (Eqs. (4.4)–(4.5)).

a precise determination of the intersecting point in the layer (Section 5.2). The calculated efficiencies incorporate information on the acceptance, and the accuracy depends on the quality of the tracking by other layers. The efficiency of a single layer of scintillating fibers is determined to be about 90% for protons (momentum about 0.3 GeV/c) and 80% for pions (momentum about 0.8 GeV/c) (Section 5.4).

Appendix A

Energy loss distribution extracted from Monte Carlo data and the corresponding particle identification results

The HERMES Monte Carlo (MC) *DISng*¹ simulates deep inelastic scattering of electrons/positrons on protons in the Recoil Detector. Using this set of MC data, knowledge about the energy loss of different types of particles, as well as about special detector response like the SciFi overflow, can be obtained.

The simulated energy loss distribution can be extracted as described in Chapter 3. Because of the limited statistics, the data sample is selected according to the generated particle types, not by the mass assumption described in Section 3.2.3. Results are shown in Fig. A.1.

The efficiency and contamination factor are then calculated as described in Chapter 4. Results are compared with those from real data (Fig. A.2).

¹The used production is documented in <http://hermes-wiki.desy.de/index.php/MC.Productions#022>.

APPENDIX A. ENERGY LOSS DISTRIBUTION EXTRACTED FROM MONTE CARLO DATA AND THE CORRESPONDING PARTICLE IDENTIFICATION RESULTS

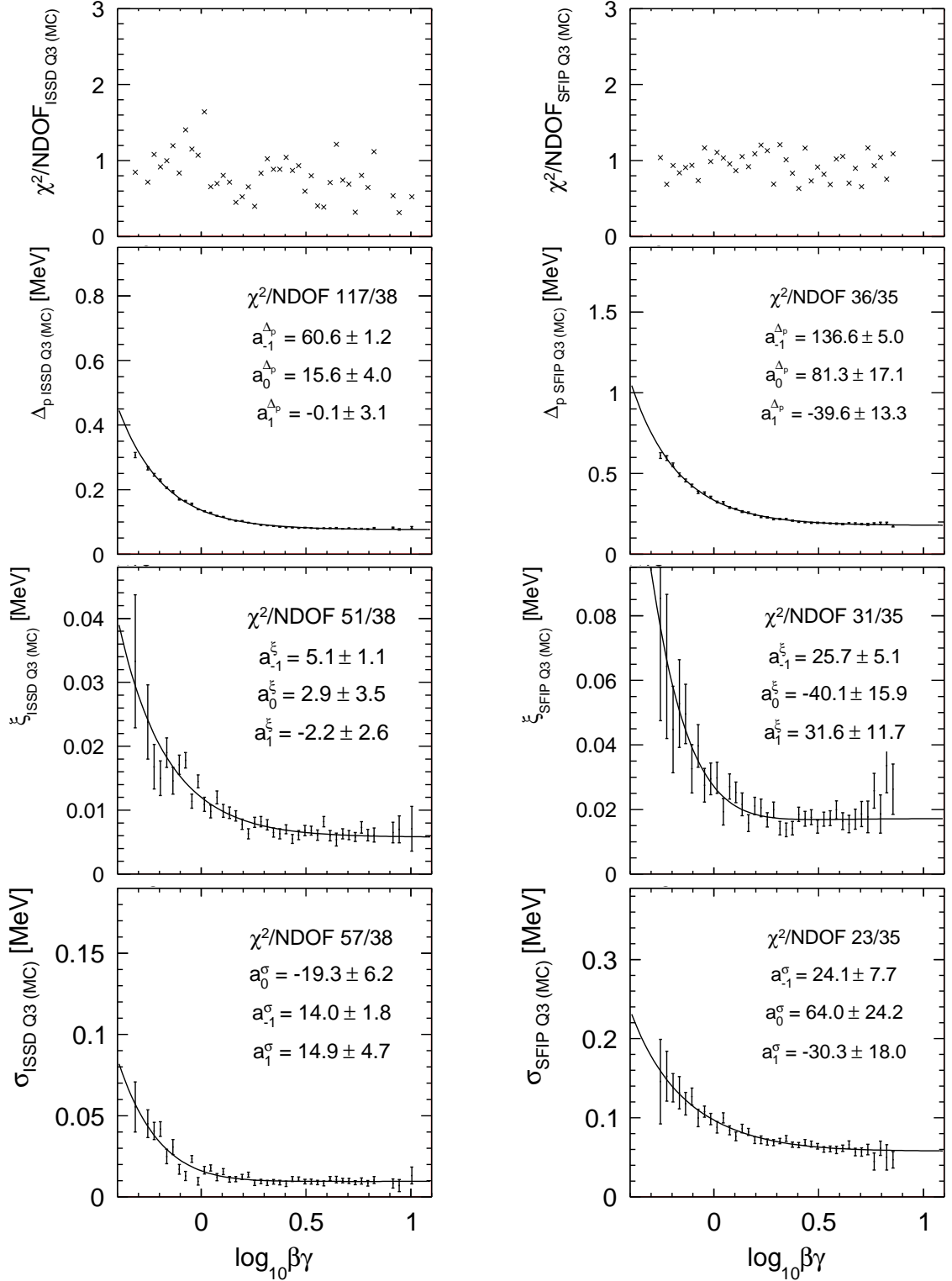


Figure A.1: *Uppermost:* the quality of fit (measured by χ^2/NDOF) to the energy loss distributions simulated in MC data. *Lower:* extracted Δ_p , ξ , σ , and the corresponding fits to them. Fitting parameters shown are in keV.

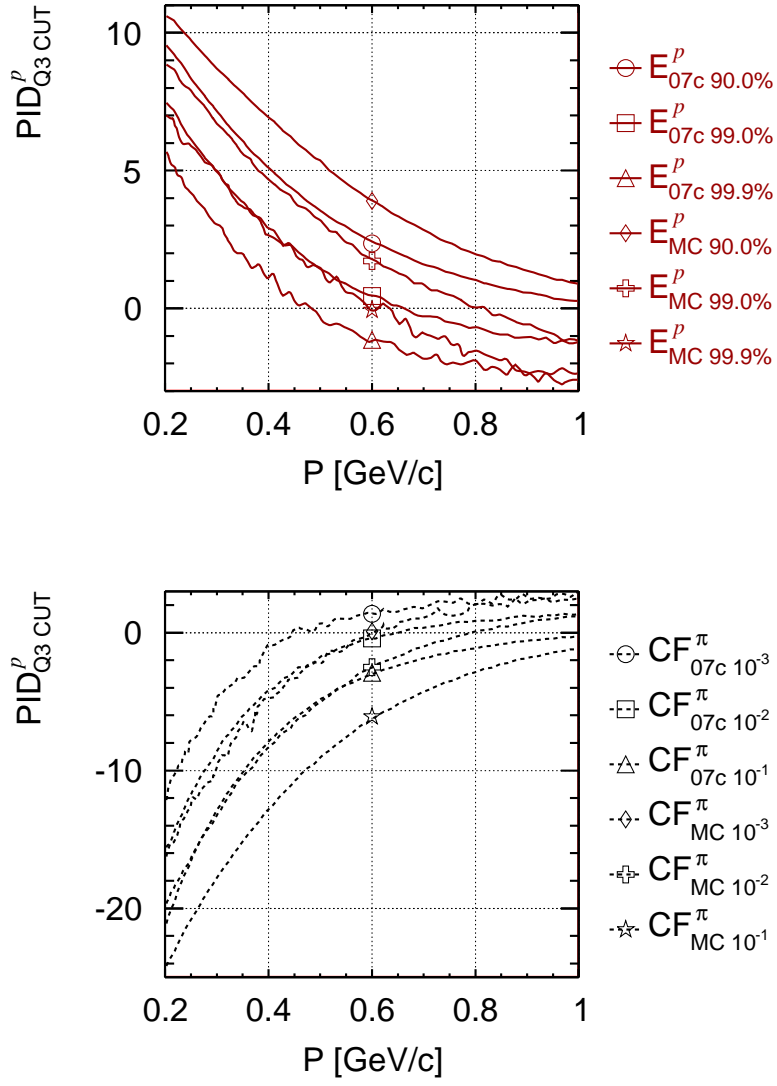
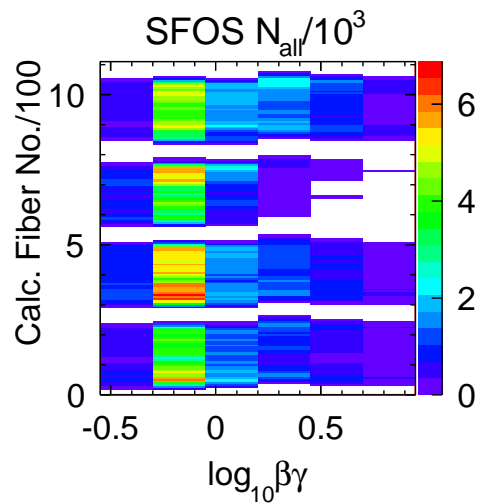
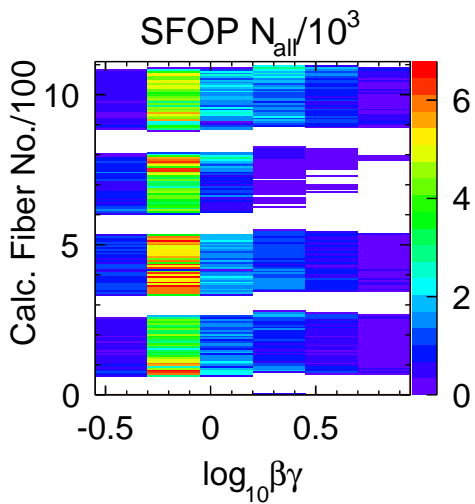
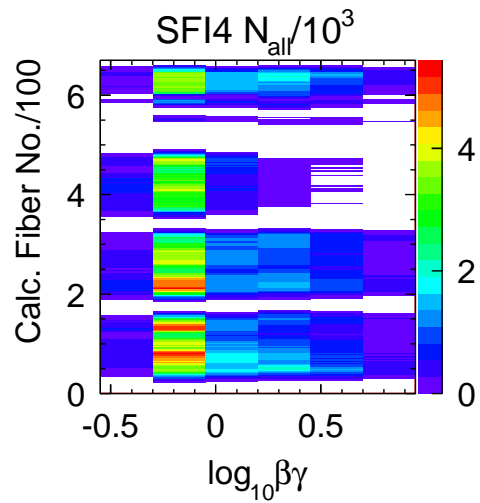
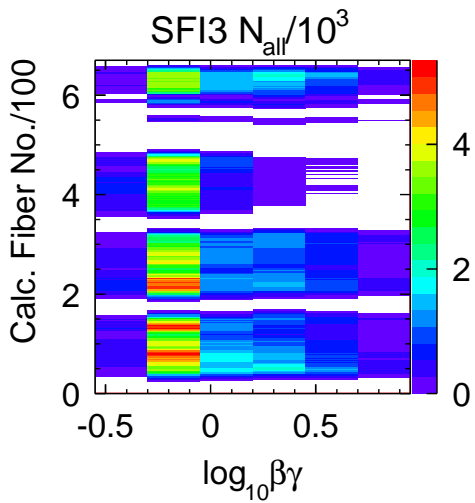
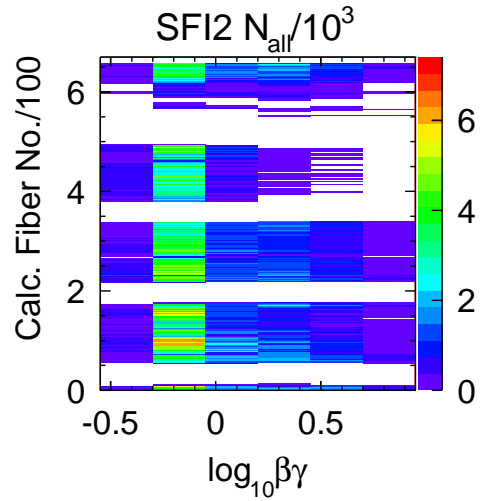
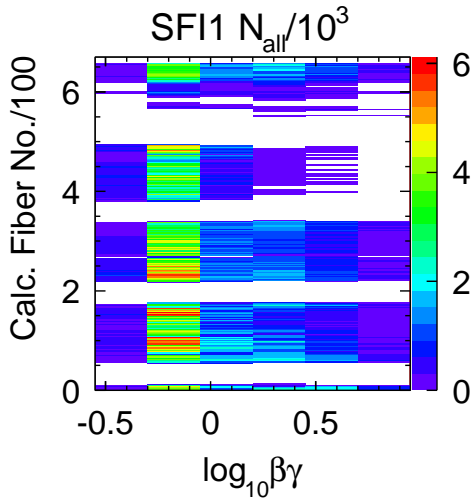


Figure A.2: Data (07c)-MC comparisons for PID_{CUT}^p .

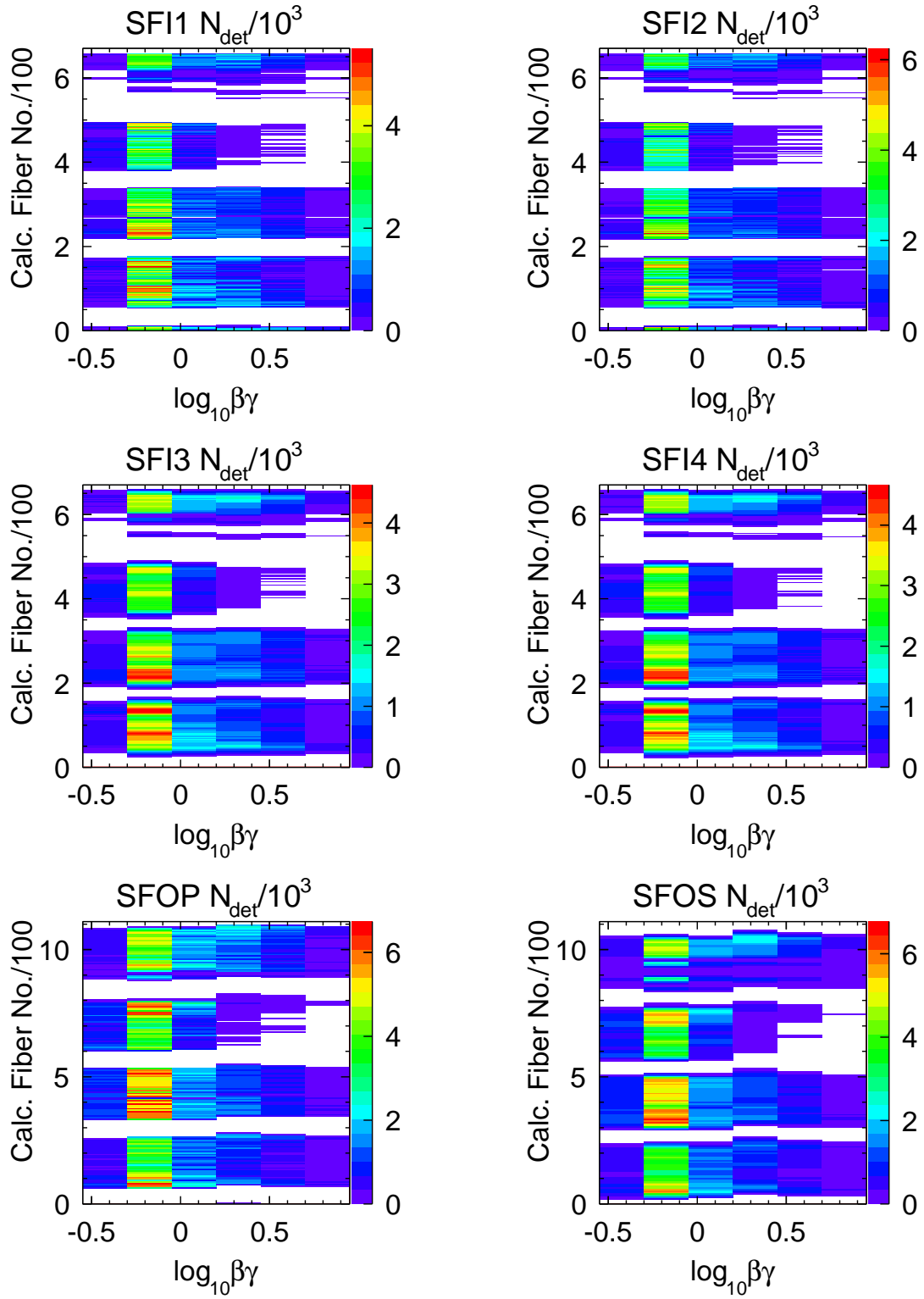
Appendix B

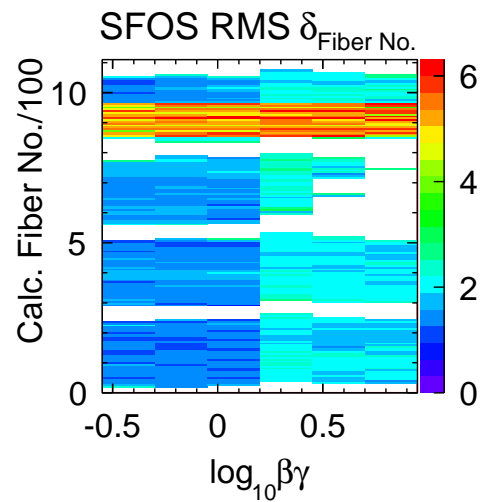
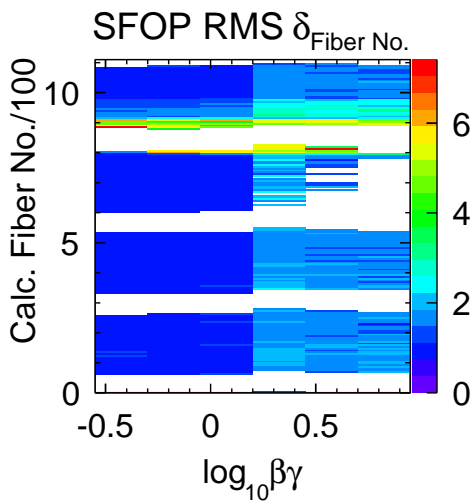
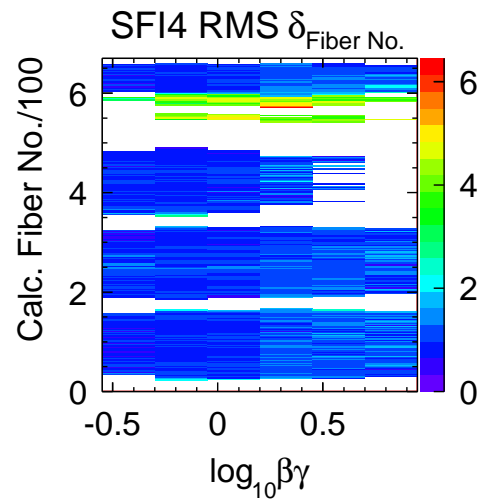
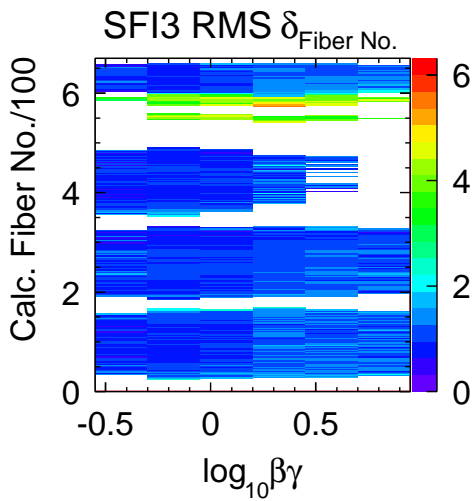
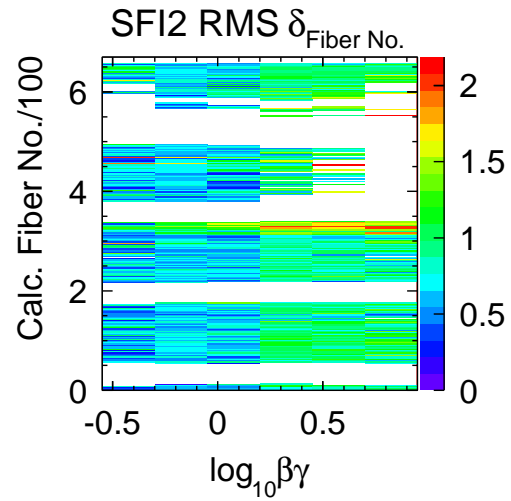
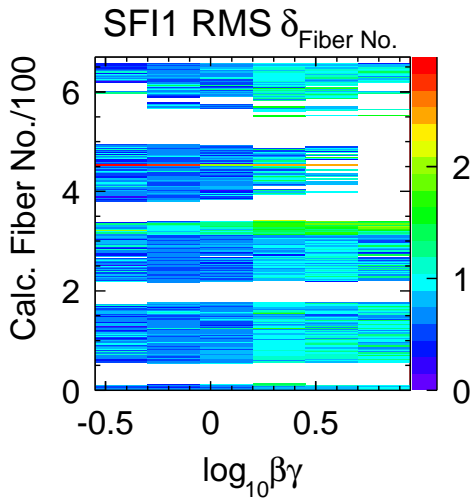
Color plots for efficiency of the scintillating fiber tracker

The following is the color version of the plots in Section 5.4.

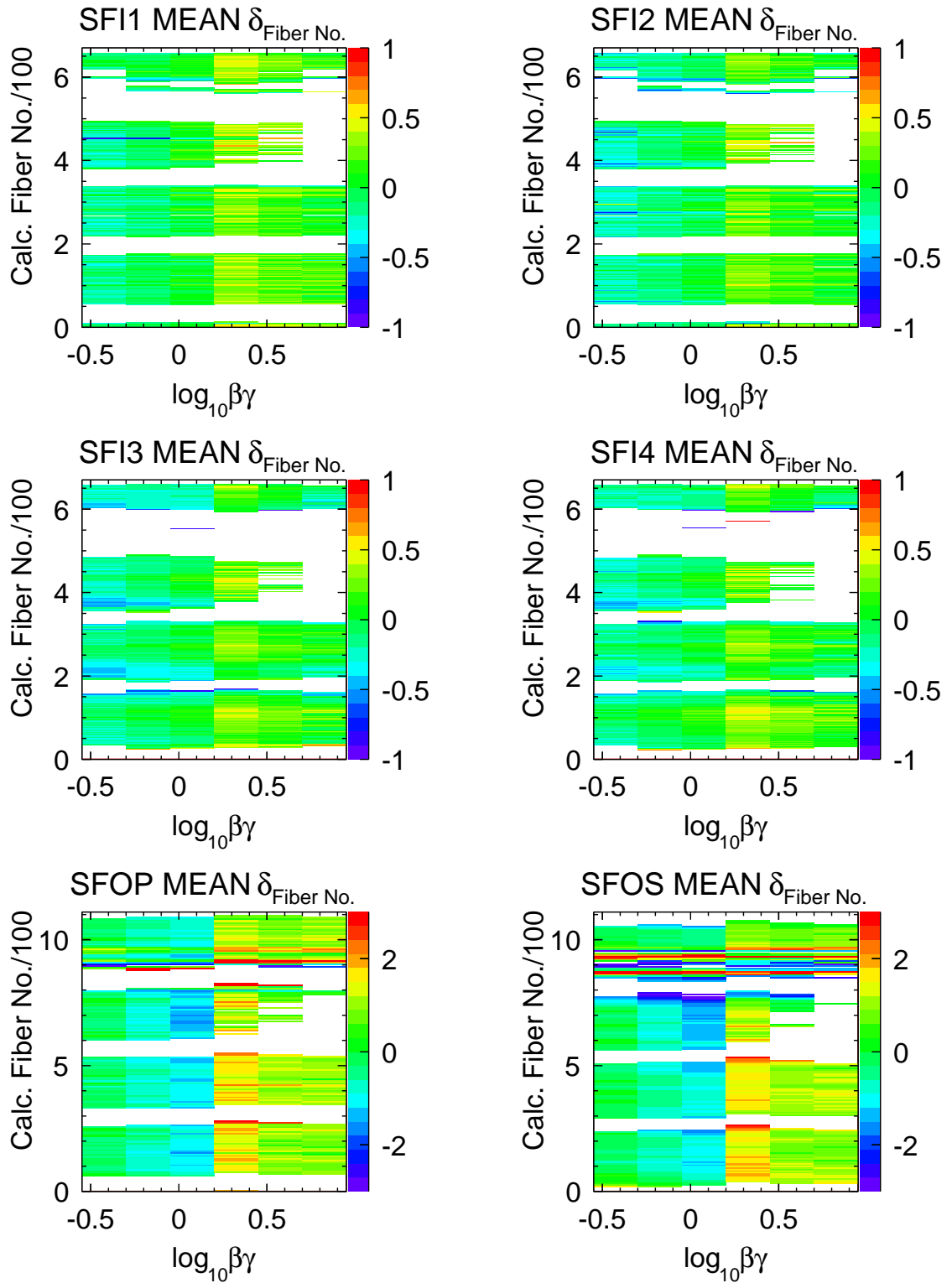


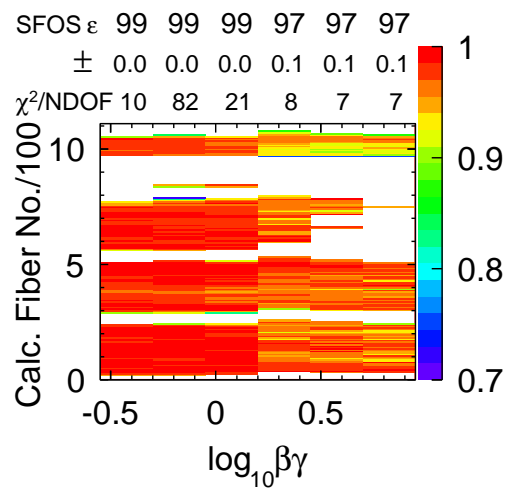
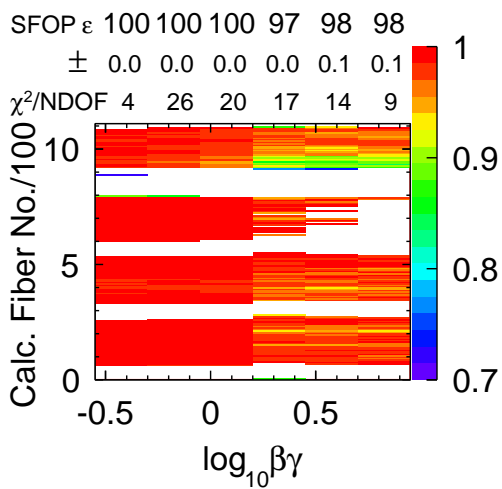
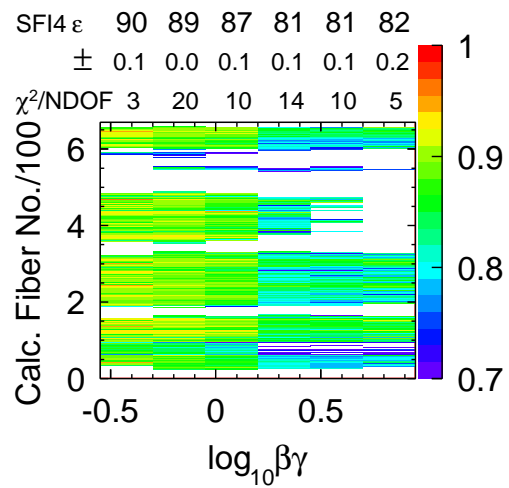
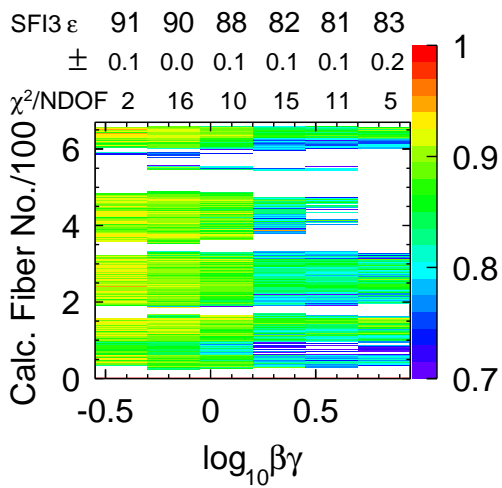
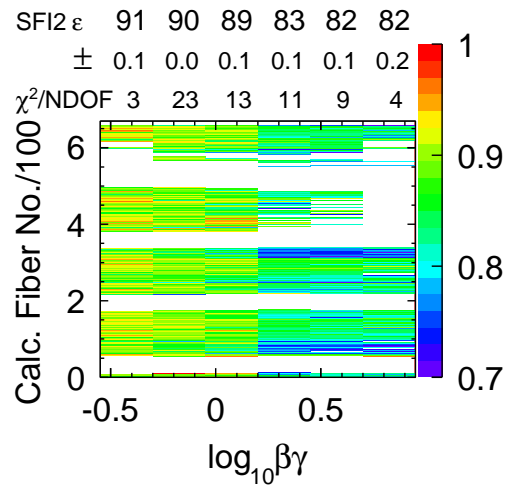
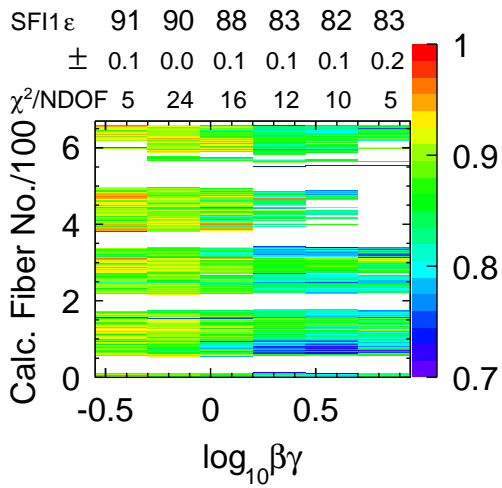
APPENDIX B. COLOR PLOTS FOR EFFICIENCY OF THE SCINTILLATING FIBER TRACKER



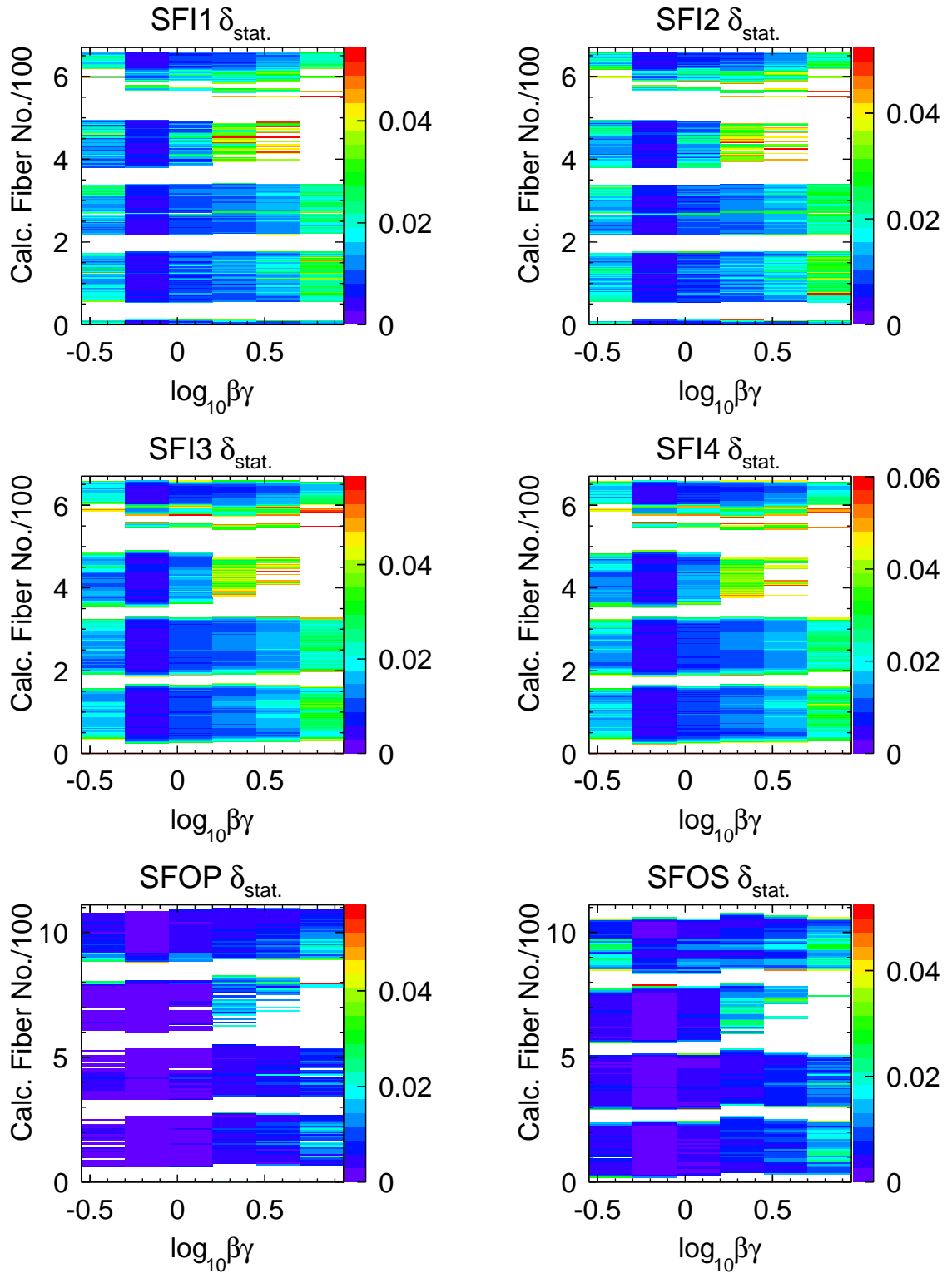


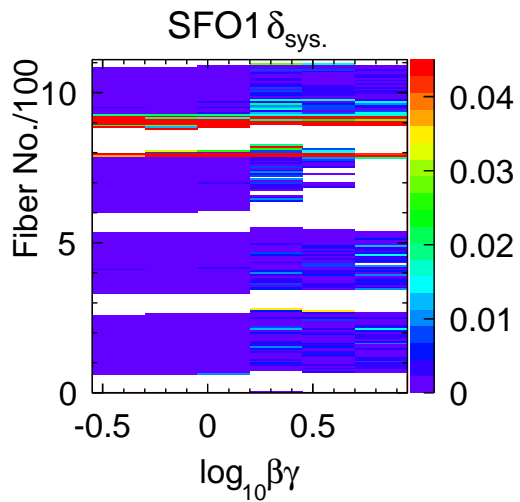
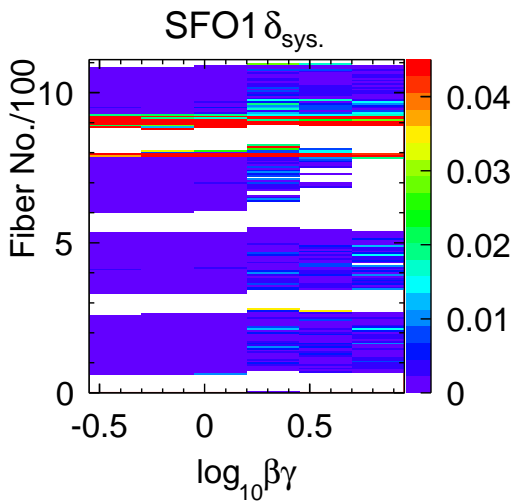
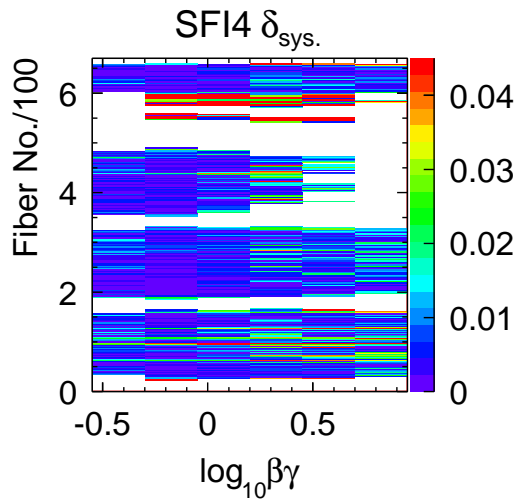
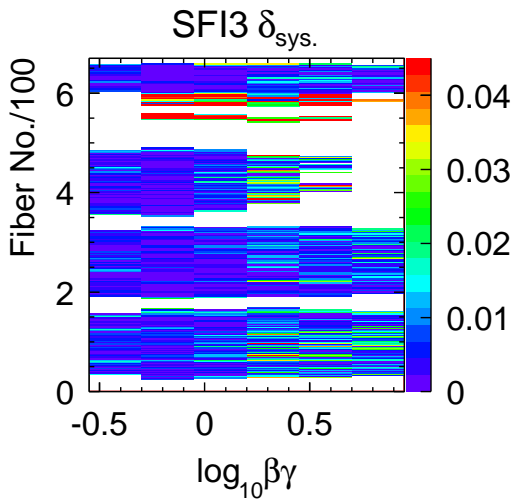
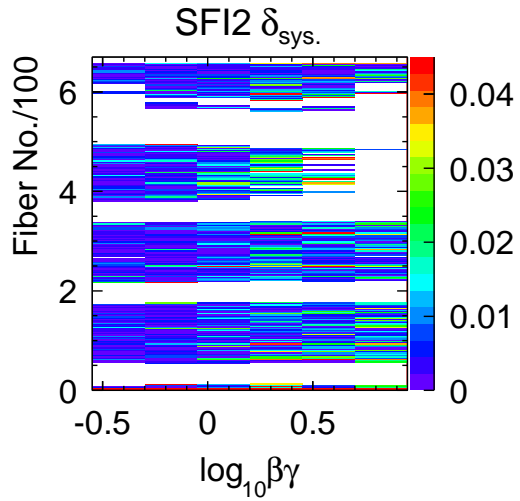
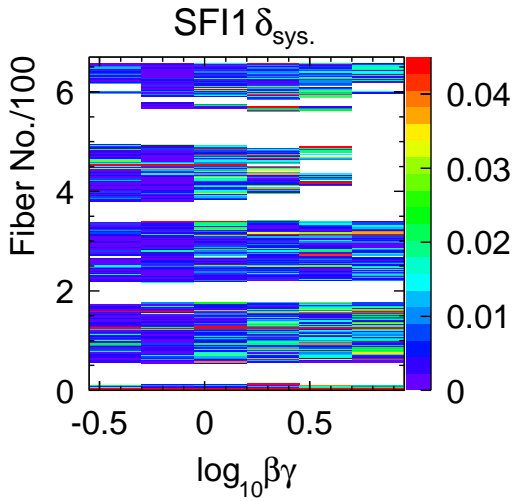
APPENDIX B. COLOR PLOTS FOR EFFICIENCY OF THE SCINTILLATING FIBER TRACKER





APPENDIX B. COLOR PLOTS FOR EFFICIENCY OF THE SCINTILLATING FIBER TRACKER





Bibliography

- [Ack98] K. Ackerstaff *et al.* [HERMES Collaboration], “HERMES spectrometer,” Nucl. Instrum. Meth. A **417**, 230 (1998) [arXiv:hep-ex/9806008].
- [Air01] A. Airapetian *et al.* [HERMES Collaboration], Phys. Rev. Lett. **87** (2001) 182001 [arXiv:hep-ex/0106068].
- [Air05] A. Airapetian *et al.* [HERMES Collaboration], Phys. Rev. D **71** (2005) 012003 [arXiv:hep-ex/0407032].
- [Air07] A. Airapetian *et al.* [HERMES Collaboration], Phys. Rev. D **75** (2007) 012007 [arXiv:hep-ex/0609039].
- [Air08] A. Airapetian *et al.* [HERMES Collaboration], JHEP **0806** (2008) 066 [arXiv:0802.2499 [hep-ex]].
- [Ams08] C. Amsler *et al.* [Particle Data Group], Phys. Lett. B **667**, 1 (2008). Related chapters: *Structure functions, Passage of particles through matter, Monte Carlo techniques, Probability.*
- [Bic88] H. Bichsel, Rev. Mod. Phys. **60**, 663 (1988).
- [Die03] M. Diehl, Phys. Rept. **388** (2003) 41 [arXiv:hep-ph/0307382].
- [Ell05] F. Ellinghaus, HERMES TRANSPARENCIES 05-099a (2005).
- [Fan63] U. Fano, Annu. Rev. Nucl. Sci. **13**, 1-66 (1963).
- [Goe01] K. Goeke, M. V. Polyakov and M. Vanderhaeghen, Prog. Part. Nucl. Phys. **47** (2001) 401 [arXiv:hep-ph/0106012].
- [Gre03] See, for example, Exercise 3.5 in QUANTUM ELECTRODYNAMICS by W. Greiner and J. Reinhardt, 3rd. ed., Springer (2003).
- [Hoe06] M. Hoek, Design and Construction of a Scintillating Fibre Tracker for measuring Hard Exclusive Reactions at HERMES, PhD thesis, Justus-Liebig-Universität Gießen (2006) [DESY-THESIS-2006-027].
- [Hu65] E. B. Hughes, T. A. Griffy, M. R. Yearian and R. Hofstadter, Phys. Rev. **139** (1965) B458.

- [Ji97] X. D. Ji, Phys. Rev. Lett. **78**, 610 (1997) [arXiv:hep-ph/9603249].
- [Ji98] X. D. Ji, J. Phys. G **24**, 1181 (1998) [arXiv:hep-ph/9807358].
- [Kai02] R. Kaiser ed., [HERMES Collaboration], The HERMES Recoil Detector Technical Design Report, DESY PRC 02-01 (2002).
- [Lu08] X.-G. Lu, Particle Identification with the Recoil-Detector at the HERMES-Experiment, talk at 40. Herbstschule für Hochenergiephysik Maria Laach (2008).
- [Men97] F. Menden, Measurement of the Valence Quark Spin Distributions of the Nucleon Using Deep Inelastic Scattering at HERMES, Diploma Thesis, Universität Hamburg (1997).
- [Mus08] A. Mussgiller, [HERMES Collaboration], PoS **VERTEX 2008**, 003 (2008).
- [Mus09] private communication, A. Mussgiller (2009).
- [Pic08] N. Pickert, Commissioning of the Recoil Silicon Detector for the HERMES Experiment, PhD thesis, Friedrich-Alexander-Universität Erlangen-Nürnberg (2008) [DESY-THESIS-2008-005].
- [Pes95] See, for example, Section 18.5 in An introduction to quantum field theory by M. Peskin, D. Schroeder, Addison-Wesley (1995).
- [Ren97] R. Brun and F. Rademakers, ROOT - An Object Oriented Data Analysis Framework, Proceedings AIHENP'96 Workshop, Lausanne, Sep. 1996, Nucl. Instrum. Meth. in Phys. Res. A **389** (1997) 81-86. See also <http://root.cern.ch/>.
- [Sau99] P. R. B. Saull [ZEUS Collaboration], arXiv:hep-ex/0003030.
- [Ste01] S. Stepanyan *et al.* [CLAS Collaboration], Phys. Rev. Lett. **87**, 182002 (2001) [arXiv:hep-ex/0107043].
- [Ste05] H. Stenzel, Alignment of the SciFi Detector at the DESY22 electron testbeam, HERMES Internal Report 05-063 (2005).
- [Van07] Y. Van Haarlem, The HERMES recoil photon-detector and nuclear pt-broadening at HERMES, PhD thesis, Universiteit Gent (2007) [DESY-THESIS-2007-033].
- [Yas09] private communications, S. Yaschenko (2009).
- [Yu09] W. Yu, PhD thesis, Justus-Liebig-Universität Gießen (2009).

Acknowledgements

I would like to thank my supervisor Wolf-Dieter Nowak at DESY Zeuthen for his continuous kind support since my visit to DESY in spring 2007 when I was still an undergraduate at Peking University. During these years, it would be impossible for me to finish all the achievements without his encouragement. I would also like to thank my direct advisors Caroline Riedl and Sergey Yaschenko. Discussions with them are always interesting and helpful. This work would not have been finished without all their help.

I would like to thank my thesis advisor Prof. Peter Schleper at Universität Hamburg. His many suggestions on my studies are very helpful.

Many of the ideas in this work came out after discussions within the HERMES recoil-group. Concerning this, I would like to thank especially (and once more to my advisors) Caroline Riedl, Sergey Yaschenko, Charlotte Van Hulse, Andreas Mussgiller and Weilin Yu.

I would like to thank Markus Diehl for proofreading Section 1.1. Special thanks for his endless patience to answer my various questions.

I would also like to thank Hongxue Ye for submitting some of my job batches using his account so that I could speed up my code running by a factor of two.

I owe many thanks to my family for their understanding and support throughout these years.

Erklärung

Hiermit versichere ich, Xianguo Lu, die vorliegende Arbeit selbstständig verfasst und nur die angegebenen Quellen als Hilfsmittel verwendet zu haben. Des Weiteren erkläre ich mich mit der Veröffentlichung dieser Arbeit einverstanden.

Hamburg, den 30. 09. 2009

Xianguo Lu